UCLouvain

École polytechnique de Louvain

MRI biomarkers of success of cochlear implant therapy in patients with acquired deafness

Author : **Justine COMMERMAN**
Supervisors : **Benoît Macq**, **Laurence DRICOT**
Readers : **Ron Kupers**, **Nicolas DELINTE**, **Quentin DESSAIN**
Academic year 2024–2025
Master [120] in Biomedical Engineering

Abstract

Acquired hearing loss is a major public health concern that can be partially mitigated through cochlear implantation. However, post-implantation outcomes vary greatly between individuals. This thesis aims to evaluate the predictive value of white matter microstructural integrity on auditory performance after cochlear implantation, using diffusion magnetic resonance imaging (dMRI).

The study includes 65 implanted patients for whom audiometric scores, such as Auditory Word Recognition Score (AWRS) and Deggouj-Wathour test (DEWA), were collected pre-operatively, and at 6 and 12 months post-implantation. Pre-operative diffusion MRI scans were used to perform probabilistic tractography and extract diffusion tensor imaging (DTI) metrics from white matter tracts involved in speech comprehension and audiovisual integration.

Significant correlations were observed between DEWA scores and specific diffusion metrics (mean diffusivity (MD), radial diffusivity (RD), and axial diffusivity (AD)) within the left posterior Arcuate Fasciculus (AF) and the right Inferior Fronto-Occipital Fasciculus (IFOF), particularly at the pre-operative and 6-month stages. No significant associations were found at 12 months or with score evolution over time. A cluster-based analysis identified subregions, such as external capsule and the left superior temporal region, specifically associated with performance, highlighting the relevance of localized microstructural assessment.

These findings suggest that diffusion MRI may help predict cochlear implant outcomes in patients with acquired hearing loss and support more personalized clinical decision-making.

Acknowledgements

I would first like to thank Benoît Macq and Laurence Dricot, my supervisors, for giving me the opportunity to work on this fascinating topic, as well as for their guidance, thoughtful follow-up, and valuable feedback throughout this work.

I am also grateful to Ron Kupers for his insightful questions and helpful suggestions during the follow-up sessions.

My sincere thanks go to Anaïs Grégoire for taking the time to provide and explain her data, for her patience and advice, and for giving me the opportunity to build upon her work.

I also wish to thank Nicolas Delinte for his availability, his valuable guidance, and for his careful proofreading and corrections during the writing of this thesis.

A special thanks to Suzanne Vanderbemden for allowing me to observe audiometric testing in the field, which greatly enhanced my understanding of their practical application.

Thank you to my fellow Master's students, especially Salomé and Nicolas, for the mutual support and collaboration throughout this challenging year.

Finally, I would like to thank my parents and my sister for their patience, their support, and attentive listening throughout my academic journey.

List of Abbreviations

A1 Auditory Cortex.

AAL Automated Anatomical Labeling.

AD Axial Diffusivity.

AF Arcuate Fasciculus.

AWRS Average Word Recognition Score.

CC Corpus Callosum.

DEWA Deggouj-Wathour.

DTI Diffusion Tensor Imaging.

DWI Diffusion Weighted Imaging.

FA Fractional Anisotropy.

FDR False Discovery Rate.

FODF Fiber Orientation Distribution function.

IFOF Inferior Fronto-Occipital Fasciculus.

ILF Inferior Longitudinal Fasciculus.

MD Mean Diffusivity.

MNI Montreal Neurological Institute.

MRI Magnetic Resonance Imaging.

NMR Nuclear Magnetic Resonance.

NODDI Neurite Orientation Dispersion and Density Imaging.

RD Radial Diffusivity.

RF radiofrequency.

ROIs Regions of Interest.

SNR signal-to-noise ratio.

STG Temporal Superior Gyrus.

TE Echo Time.

TR Repetition Time.

UF Uncinate Fasciculus.

List of Figures

List of Tables

Contents

Introduction

Hearing loss represents a major global public health issue. According to the World Health Organization (WHO), over 5% of the world's population, approximately 430 million people, suffer from a disabling hearing impairment[1]. When left untreated, hearing loss can lead to various consequences, including limitations in communication, increased social isolation, reduced access to education and employment, and an overall decline in quality of life [1].

Among recent medical devices, the cochlear implant represents a major advancement for individuals with severe to profound hearing loss. It enables many patients to regain sufficient auditory perception to improve both autonomy and quality of life. However, the outcomes after implantation vary significantly from one individual to another. Some patients do not achieve the expected results, despite the high costs associated with the procedure, although partially reimbursed in Belgium [2], and the considerable effort required for rehabilitation.

It is therefore essential to be able to predict, prior to surgery, the chances of success of a cochlear implant for a given patient. Such an evaluation would not only help optimize surgical indications but also spare certain patients from undergoing an invasive procedure and demanding rehabilitation with limited benefits. Yet, most current studies focus on congenital deafness, while acquired hearing loss, despite being more common, remains less explored in this context.

In the face of rising prevalence, the WHO estimates that by 2050, over 2.5 billion people will be affected by some form of hearing impairment [1], reinforcing the urgency of developing robust predictive tools. This thesis aligns with that goal: its primary objective is to evaluate the predictive value of microstructural brain measures, derived from diffusion MRI tractography, on post-implantation outcomes in patients with acquired hearing loss.

---

[1] A hearing impairment is considered disabling when it exceeds 35 decibels (dB) in the better-hearing ear [1].

Specifically, this work aims to examine correlations between diffusion tensor imaging measures and audiometric test performance after cochlear implantation. To this end, data from a sample of 65 implanted patients was analyzed, focusing on the microstructural properties of white matter pathways involved in speech, language comprehension and auditory processing.

The data include preoperative MRI scans and audiometric test scores (AWRS and DEWA), measured preoperatively and at 6 and 12 months post-implantation. Patients' age and the duration of prior hearing aid use were also considered. Probabilistic tractography was used to extract relevant metrics from tracts of interest. Spearman correlation analyses as well as partial correlation analyses were then applied to evaluate relationships between diffusion metrics, such as fractional anisotropy, and auditory performance outcomes.

This thesis is structured into two main parts. The first provides a review of the literature, including the fundamentals of MRI, principles of DTI and tractography, the anatomy of the central auditory system, types of hearing loss, cochlear implants, and audiometric evaluation tools. The second part presents the experimental study, including a detailed description of the methodology, results, a critical discussion in light of existing literature and the study's limitations, and finally a conclusion summarizing the findings.

This thesis has been partially reformulated, and translated into English with the assistance of an AI tool.

Part I

Theorical concepts

Chapter 1

Magnetic Resonance Imaging

1.1 The Principle of MRI

Magnetic Resonance Imaging (MRI) is based on the principles of Nuclear Magnetic Resonance (NMR) to obtain detailed images of the internal structures of the human body. NMR exploits the magnetic properties of atomic nuclei, particularly those of hydrogen atoms, by subjecting them to the combined action of two magnetic fields: a fixed static magnetic field, denoted B_0, which aligns the hydrogen nuclei along its direction (typically the longitudinal z-axis), and a rotating electromagnetic field, denoted B_1, which excites these nuclei and induces a measurable signal.

1.1.1 Magnetic Properties

Magnetic Properties of Hydrogen

Among all atomic nuclei, hydrogen is particularly relevant in MRI due to its abundance in the human body and its strong magnetic properties. Hydrogen makes up approximately 70% of the human body, has a high intrinsic magnetic moment, and exhibits a well-defined nuclear magnetic resonance. Each hydrogen atom consists of a single proton and can be characterized by its spin. This spin, or angular momentum, is induced by the individual rotation of the particle around an axis passing through its center, represented by the vector S in Figure 1.1 [3].

In the absence of an external magnetic field, the magnetic moments of hydrogen protons are randomly oriented, and the net magnetization vector is effectively zero. However, when placed in an external magnetic field B_0, these magnetic moments tend to align with or against the field direction. This creates two energy states: a low-energy state (parallel to B_0) and a high-energy state (antiparallel to B_0). Although both orientations exist, there is a slight excess of protons in the lower energy state, resulting in a net macroscopic magnetization vector denoted as M parallel to B_0 [3].

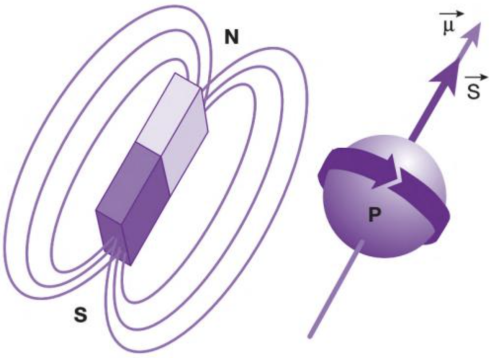

Figure 1.1: Representation of the magnetic moment ($\vec{\mu}$) and angular momentum (or spin, $\vec{S}$) of a proton. The magnetic moment behaves like a dipole, with a north (**N**) and a south (**S**) pole [3].

Effect of the External Magnetic Field and Precession Frequency

When a tissue is subjected to an external magnetic field B_0, the protons gradually align along the direction of this field. However, this alignment is not perfect: instead of remaining stationary, the protons precess around the axis of the B_0 field at a specific frequency, called the Larmor frequency. This frequency is defined by the equation:

$$\omega_0 = B_0 \gamma, \tag{1.1}$$

where ω_0 is the angular precession frequency, γ is the gyromagnetic ratio (specific to each type of nucleus), and B_0 is the strength of the applied magnetic field. In other words, protons rotate individually around the direction of B_0 with a specific precession angle and at angular precession frequency ω_0, as illustrated in Figure 1.2 [3].

Components of the Magnetization Vector

In an external magnetic field, the macroscopic magnetization vector M has two distinct components, defined as follows:

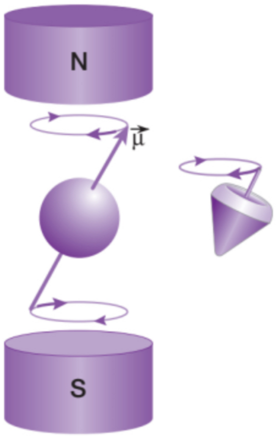

Figure 1.2: Schematic representation of proton precession. When exposed to an external magnetic field B_0, protons partially align and precess around the field axis with a specific precession angle, defined by their magnetic moment $\vec{\mu}$ [3].

$$M = M_z \mathbf{1}_z + M_{xy} \mathbf{1}_{xy}$$

Before excitation, the net magnetization vector is exclusively aligned with the static magnetic field B_0, along the O_z axis. This component is referred to as longitudinal magnetization M_z. At equilibrium, the transverse component M_{xy}, which lies in the plane perpendicular to B_0, is null because individual protons precess in a disorganized and dephased manner. In other words, $M_{xy} = 0$ and $M_z \neq 0$, meaning magnetization is exclusively longitudinal, as illustrated in Figure 1.3. However, this equilibrium magnetization along the O_z axis cannot be directly measured, as it is too weak compared to the B_0 field.

Radiofrequency Excitation

To make the magnetization detectable, a second rotating magnetic field B_1 is applied perpendicular to B_0, along the O_x axis. This wave transfers the magnetization into the transverse plane O_{xy}, thereby generating a measurable signal detected by the MRI receiver coils.

A measurable signal can only be produced by disturbing the system's equilibrium through energy transfer, typically achieved by applying a second magnetic field. This transfer is only effective if resonance occurs, meaning the frequency of the applied rotating field ω_r equals the Larmor frequency ω_0. Since

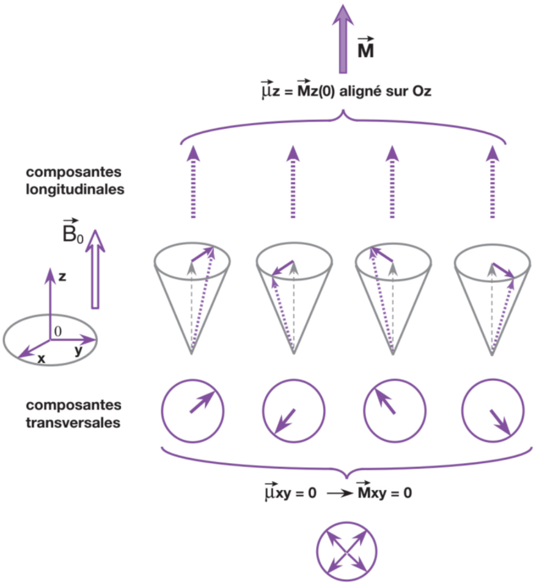

Figure 1.3: Schematic representation of proton alignment and precession at equilibrium. At equilibrium, protons align along the B_0 field while undergoing a precession motion around it at a certain angle. This results in the presence of a longitudinal magnetization component M_z. In contrast, the transverse component M_{xy} is absent due to proton dephasing [3].

ω_0 is directly proportional to the strength of the main magnetic field B_0 (see Equation 1.1), the excitation field B_1 must operate at a frequency that also lies within the radiofrequency (RF) range. In clinical MRI, typical B_0 field strengths are 1.5 T and 3 T, corresponding to Larmor frequencies of approximately 64 MHz and 128 MHz, respectively.

When the electromagnetic field B_1, or RF wave, is applied, the macroscopic vector M continues to precess around B_0 along O_z at the angular frequency ω_0, but it also begins to precess around B_1 along O_x at the angular frequency ω_1.
In practice, the application of this RF wave is brief, lasting only a few milliseconds. It causes the appearance of a transverse magnetization component through proton rephasing. Its effect is to tilt the magnetization vector M by a specific angle, typically 90° or 180°. This phenomenon is referred to as a radiofrequency pulse or excitation. To obtain a 180° pulse, the RF pulse must be applied for twice as long or at twice the intensity compared to a 90° pulse. RF pulses are schematically illustrated in Figure 1.4 [3].

Once the RF pulse is turned off, the system no longer receives energy and begins to return to its equilibrium state. This return process, during which the magnetization vector recovers its initial configuration, is known as relaxation. It is during this phase that the MRI signal is measured and image contrast is generated, as described in the following section.

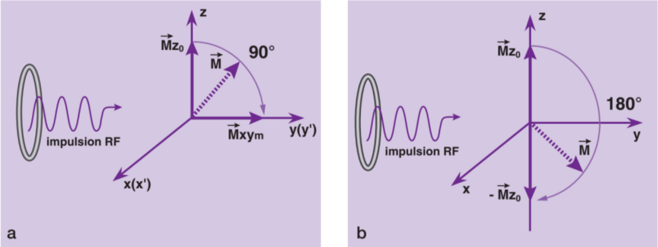

Figure 1.4: Representation of the effect of RF pulses on the macroscopic magnetization vector M. (a) A 90° RF pulse rotates the magnetization from the longitudinal axis (M_z) into the transverse plane (M_{xy}), making it detectable. (b) A 180° RF pulse inverts the magnetization, flipping it from $+M_z$ to $-M_z$. Both pulses are applied perpendicular to the static magnetic field B_0 and induce precession at the Larmor frequency [3].

1.1.2 The Relaxation Phenomenon

The relaxation time refers to the duration allowed for protons to return to their stable state after being flipped by 90° or 180° due to the RF pulse. It is during this relaxation process that the measurements are taken. Indeed, because different tissues in the body have their own specific relaxation times, this enables the observation of contrast in the resulting images and thus the identification of anatomical structures.

Once the excitation ends, the system gradually returns to equilibrium through two distinct relaxation processes. First, the protons that had absorbed energy revert to a lower energy state, leading to the recovery of longitudinal magnetization M_z. This process is known as T_1 relaxation. At the same time, the transverse magnetization M_{xy} rapidly decays, as the spins that were previously synchronized lose coherence and fall out of phase. This phenomenon is referred to as T_2 relaxation.

Longitudinal Relaxation or T_1

After excitation by a RF pulse, the gradual return of protons to their equilibrium state along the axis of the magnetic field B_0 is called longitudinal relaxation, or T_1 relaxation. This phenomenon corresponds to the recovery of longitudinal magnetization M_z through energy exchange with the molecular environment.

The duration of this recovery, characterized by the T_1 relaxation time, varies depending on the nature of the tissue. In general, fatty tissues have a short T_1, as energy is quickly transferred. Moreover, liquids have a longer T_1 than solids, due to less efficient molecular interactions for energy exchange.

The evolution of longitudinal magnetization over time follows an exponential growth model (see Figure 1.5), mathematically described by the equation:

$$M(t) = M_0(1 - e^{\frac{-t}{T_1}}).$$

At $t = T_1$, the magnetization reaches approximately 63% of its maximum value M_0. This is because the factor e^{-1} is approximately 0.37, and thus: $1 - e^{-1} \approx 0.63$ Therefore, the T_1 time corresponds to the moment when 63% of the longitudinal magnetization has been restored [4].

Transverse Relaxation or T_2

Following a 90° RF pulse, the protons momentarily align in phase, producing maximal transverse magnetization M_{xy}. However, this synchronized state is unstable. Almost immediately, the protons begin to lose coherence due to spin-spin interactions and small variations in the local magnetic field. This process, known as transverse relaxation T_2, leads to a gradual reduction of M_{xy}, which decreases according to an exponential decay curve.

The T_2 relaxation time characterizes the speed of this dephasing: T_2 is short in solid tissues, where spin interactions are strong, and longer in liquids, where these interactions are weaker. The evolution of transverse magnetization over time is described by the following equation (see figure 1.5):

$$M_{xy}(t) = M_{xy}(0)e^{\frac{-t}{T_2}}$$

where $M_{xy}(0)$ is the transverse magnetization immediately after excitation, and $M_{xy}(t)$ its value at time t. Therefore, at $t = T_2$, about 63% of the initial transverse magnetization has decayed, meaning that only approximately 37% of $M_{xy}(0)$ remains. This exponential decay reflects the loss of phase coherence among spins. It is considered that 63% of transverse magnetization has decayed after a T_2 time [4].

1.1.3 Spin Echo

The spin echo sequence is an MRI technique based on the application of two successive RF pulses. First, an initial 90° pulse is applied to flip the longitudinal magnetization into the transverse plane. After a delay of Echo Time (TE) divided

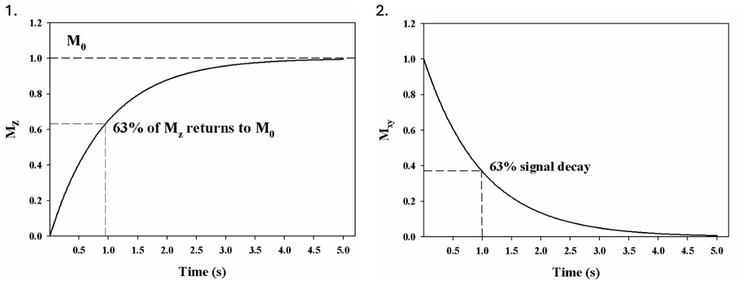

Figure 1.5: Evolution of magnetization during relaxation processes.(1) Longitudinal relaxation: the longitudinal magnetization M_z progressively returns to its equilibrium value M_0 following an exponential growth curve. After a time equal to T_1, approximately 63% of M_z has recovered. (2) Transverse relaxation: the transverse magnetization M_{xy} decays exponentially due to dephasing phenomena. After a time equal to T_2, about 63% of the initial transverse magnetization has decayed [4].

by 2, TE/2, a second 180° pulse is delivered to rephase the spins and compensate for inhomogeneities in the static magnetic field B_0. This correction generates an echo signal, which is recorded at the TE, corresponding to the moment when transverse magnetization is maximal. This sequence is illustrated in Figure 1.6.

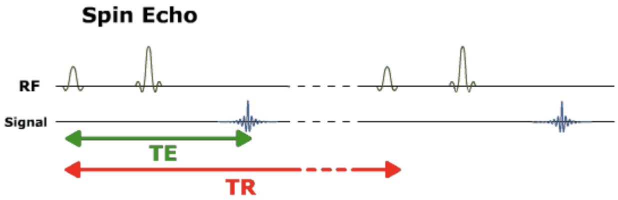

Figure 1.6: Diagram illustrating the Spin Echo sequence. A 90° RF pulse is followed by a 180° RF pulse, generating an echo signal at time TE. Repetition Time (TR) represents the interval between successive 90° excitations [5].

Two key parameters define this sequence: the repetition time and the echo time. TR is the interval between two successive 90° excitations and determines the evolution of longitudinal relaxation. The shorter the TR, the more limited the recovery of longitudinal magnetization, favoring T_1 weighting. In contrast, a long TR allows complete tissue relaxation, thereby reducing the influence of T_1 in the final contrast.

TE, on the other hand, is the time interval between the 90° pulse and the measured signal. It directly influences the decay of transverse magnetization and thus determines T_2 weighting. A short TE limits T_2 effects and results in an image closer to T_1 weighting, while a long TE enhances contrasts based on transverse

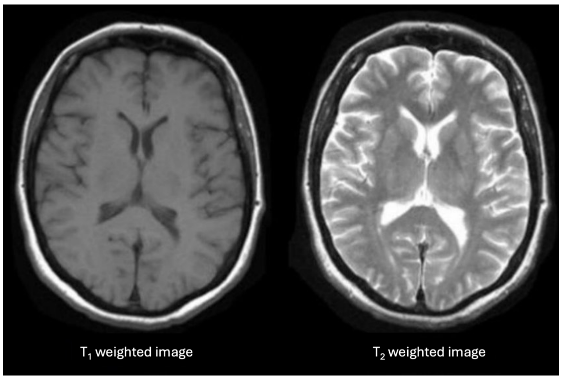

Figure 1.7: Comparison between T_1-weighted (left) and T_2-weighted (right) MRI images. In T_1 weighting, fat appears bright and water dark; in T_2 weighting, water appears bright and fat darker. These contrasts help distinguish tissue types [8].

relaxation, allowing better visualization of water-rich structures [6].

By adjusting these two parameters, different image weightings can be achieved. In T_1-weighted imaging (short TR and short TE), fat appears bright and water dark. In T_2-weighted imaging (long TR and long TE), water becomes hyperintense while fat appears relatively darker, as shown in Figure 1.7). This distinction is particularly useful for differentiating tissues and detecting certain pathologies, especially inflammatory and edematous lesions [7].

While T_1- and T_2-weighted sequences are fundamental for anatomical imaging and detecting lesions, they generate contrast based on how different tissues relax after excitation. More advanced MRI techniques, however, can go beyond these relaxation properties to explore additional tissue characteristics, such as the microscopic movement of water molecules. One such technique is Diffusion Weighted Imaging (DWI), which offers valuable insight into the microstructural environment by measuring how water diffuses within tissues.

1.2 Diffusion Weighted Imaging

DWI is an MRI sequence that is sensitive to the microscopic random motion of water molecules, particularly protons. This motion, called diffusion, results from the spontaneous displacement of molecules due to Brownian motion [9, 10].

Two types of diffusion can be distinguished: isotropic diffusion, where molecules move freely in all directions (as in cerebrospinal fluid), and anisotropic diffusion,

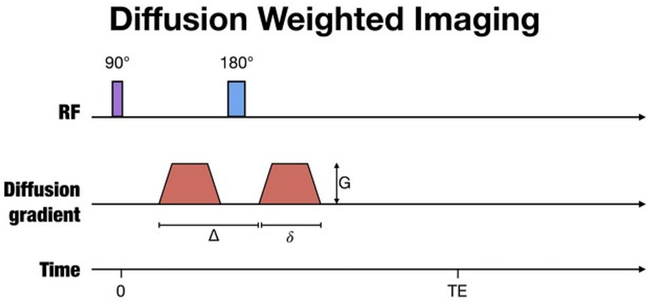

Figure 1.8: DWI sequence illustrating the application of diffusion gradients, where γ is the gyromagnetic ratio, G the gradient magnitude, δ their duration, and Δ the interval between the two gradients [11].

where movement is restricted by surrounding structures such as cell membranes or white matter fiber bundles.

DWI is based on the application of two magnetic gradients of equal intensity but opposite polarity, surrounding a RF pulse (see Figure 1.8). If the protons remain stationary between the two gradients, the phase effects are canceled and a strong signal is detected. In contrast, if the protons have diffused during this interval, their phases become incoherent and the signal is attenuated. Thus, regions with restricted diffusion appear bright, while areas of free diffusion, such as the cerebral ventricles, appear dark.

To quantify how strongly the DWI sequence reacts to diffusion, the b-value is introduced. Indeed, the intensity of diffusion sensitivity is determined by the b-value, which depends on several physical parameters of the gradient, according to the following formula:

$$b = \gamma^2 G^2 \delta^2 \left(\Delta - \frac{\delta}{3} \right)$$

where γ is the gyromagnetic ratio, G the gradient magnitude, δ their duration, and Δ the interval between the two gradients. Therefore, a high b-value increases sensitivity to diffusive motion (see Figure 1.9). This increase in diffusion sensitivity leads to signal attenuation, which follows the exponential relationship:

$$S = S_0 e^{-bD}$$

where S_0 is the reference signal without diffusion, depending on T_2-weighted image, and D is the apparent diffusion coefficient [12].

Each voxel represents a small tissue volume, and DWI evaluates water diffusion along the three spatial axes (x, y, and z). The recorded signals are then compared

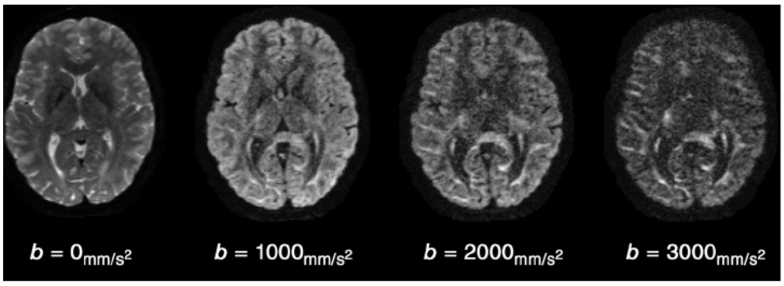

Figure 1.9: Series of brain MRI images acquired with increasing diffusion weighting. As the b-value increases, signal attenuation becomes more pronounced in areas of free diffusion, enhancing the contrast in regions with restricted diffusion [12].

to a T_2-weighted reference image. In the case of free diffusion, at least one direction shows signal attenuation; in contrast, if all three directions retain high signal intensity, this indicates diffusion restriction, which appears as a white region on the image. Due to the long echo time required by DWI sequences, the resulting images also exhibit a T_2-weighted contrast component. This combination makes DWI particularly sensitive for the early detection of acute cerebral infarctions, where diffusion is abruptly restricted.

However, DWI is also susceptible to motion artifacts. Involuntary macroscopic movements, such as cardiac pulsations, respiration, or slight patient motion, can cause signal dephasing, leading to image distortions like blurring or ghosting [10].

In summary, DWI provides a powerful contrast mechanism based on the mobility of water molecules, enabling early detection of pathological changes in tissue microstructure. Nevertheless, it does not provide information about the directionality of diffusion. To address this limitation, Diffusion Tensor Imaging (DTI) was developed.

1.2.1 Diffusion Tensor Imaging

DTI is a method derived from DWI that allows the representation of anisotropic water diffusion in tissues using a diffusion tensor. This mathematical model, expressed as a 3x3 matrix (Equation 1.2), describes diffusion displacements along the x, y, and z axes, taking into account both their direction and intensity. It enables the representation of both isotropic and anisotropic diffusion in three-dimensional space. This symmetric and positive-definite matrix can be decomposed into three orthogonal eigenvectors and three associated positive eigenvalues, denoted λ_1, λ_2, and λ_3. The major eigenvector defines the principal direction of diffusion and is often aligned with the main axis of fiber bundles in white matter. Together,

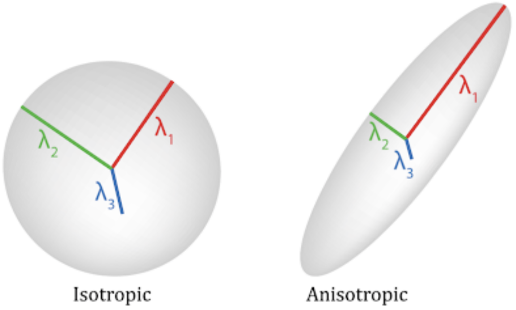

Figure 1.10: Visualization of diffusion ellipsoids and principal diffusion directions. On the left, an isotropic tensor, where the three eigenvalues λ_1, λ_2, and λ_3 have the same magnitude, indicating equal diffusion in all directions. On the right, an anisotropic tensor, where $\lambda_1 \gg \lambda_2 \approx \lambda_3$, indicating preferential diffusion along a principal axis [16].

the three eigenvectors form a local coordinate system that reflects the underlying fiber geometry, assuming no crossing, fanning, or branching of tracts within the voxel [13].

$$D = \begin{pmatrix} D_{xx} & D_{xy} & D_{xz} \\ D_{yx} & D_{yy} & D_{yz} \\ D_{zx} & D_{zy} & D_{zz} \end{pmatrix} \tag{1.2}$$

DTI provides an indirect representation of the orientation and anisotropy of fibrous structures, particularly white matter tracts. Each voxel contains a model of the local microstructure, which allows mapping of tissue organization and exploration of brain connectivity through tractography [9, 14, 15]. The principal diffusion direction is used to infer the direction of nerve fibers. This direction is color-coded according to a standard convention: red for right-left, green for anterior–posterior, and blue for inferior–superior orientations. The tensor can be visually represented using ellipsoidal glyphs, where the principal axis corresponds to the dominant diffusion direction, and the secondary axes indicate more restricted directions. This visualization makes it possible to locally estimate the fiber trajectory within each voxel (see Figure 1.10).

From the tensor, several scalar measures can be calculated to quantify diffusion:

- **Fractional Anisotropy (FA)**: indicates the degree of diffusion directionality;
- **Mean Diffusivity (MD)**: average of diffusional displacements in all directions;
- **Axial Diffusivity (AD)**: diffusion along the main direction;
- **Radial Diffusivity (RD)**: average diffusion perpendicular to the main axis.

These measures are derived from the three eigenvalues of the diffusion tensor. These eigenvalues allow the inference of microstructural characteristics such as fiber density, thickness, organization, and degree of myelination [15, 17].

The mathematical relationships between the eigenvalues and the indices are as follows:

$$\begin{aligned} AD &= \lambda_1 \\ MD &= \frac{\lambda_1 + \lambda_2 + \lambda_3}{3} \\ RD &= \frac{\lambda_2 + \lambda_3}{2} \\ FA &= \sqrt{\frac{1}{2}} \cdot \frac{\sqrt{(\lambda_1 - \lambda_2)^2 + (\lambda_1 - \lambda_3)^2 + (\lambda_2 - \lambda_3)^2}}{\sqrt{\lambda_1^2 + \lambda_2^2 + \lambda_3^2}} \end{aligned} \tag{1.3}$$

Among these measures, Fractional Anisotropy (FA) is particularly valuable as a non-invasive biomarker of white matter tract integrity, and is widely used in the study of neurological and psychiatric disorders [17, 18].

1.2.2 Limitations and Artifacts

As previously noted, diffusion-weighted imaging (DWI) is particularly sensitive to motion. This section provides a more detailed overview of the main technical limitations and sources of artifacts, along with commonly used strategies to minimize their impact.

One of the main technical challenges of DWI is its high sensitivity to motion. As diffusion-weighted sequences are designed to detect microscopic water displacement, they are also susceptible to small-scale macroscopic movements. Even minimal shifts in brain position during diffusion encoding can cause phase errors, leading to visible artifacts such as ghosting [10]. These movements may result from involuntary patient motion or physiological sources like brain pulsation. Such disturbances can significantly degrade image quality and limit the reliability of interpretation in clinical and research settings. To mitigate these effects, several methods are commonly employed, including head stabilization systems, shorter scan durations, retrospective motion correction techniques, and gating procedures [19].

Another well-known source of artifact is the presence of eddy currents—electrical currents that are unintentionally induced by the rapid switching of gradient fields. These can distort the spatial encoding of the MR signal and lead to inaccuracies in the derived diffusion measures. Solutions include active shielding of the gradient coils or adjusting the waveform shapes to account for these effects. In the present study, eddy current-related distortions were corrected using the Eddy algorithm from the FMRIB Software Library (FSL) [19–22].

Partial volume effects also represent a significant limitation in diffusion imaging. They appear when a voxel contains a mixture of different tissue types, such as white matter and cerebrospinal fluid (CSF) or overlapping fiber orientations. In this case, the diffusion signal reflects an average of these components, which can mask the true microstructural features. A common strategy to minimize this effect is to improve spatial resolution, for example by using smaller voxels or thinner slices [23].

Additionally, diffusion MRI suffers from inherently low signal-to-noise ratio (SNR), especially at high b-values. Low SNR reduces the reliability of estimated diffusion metrics and can result in incorrect fiber orientation estimates. Although increasing acquisition time or reducing spatial resolution can help improve SNR, these solutions introduce other trade-offs, including increased susceptibility to motion artifacts [23, 24].

The diffusion tensor model itself also comes with conceptual limitations. It assumes that diffusion within each voxel is Gaussian and that there is only one dominant fiber direction—assumptions that are often violated in regions with complex fiber architecture, such as areas of crossing or converging fibers [24]. To overcome this, alternative models such as Diffusion Kurtosis Imaging (DKI) have been developed. DKI captures deviations from Gaussian diffusion and provides a more nuanced description of tissue structure, allowing for better characterization of microstructural heterogeneity and complex fiber configurations within a voxel [25].

Despite these technical and conceptual constraints, diffusion MRI remains a powerful method for investigating white matter organization. By analyzing the principal diffusion direction in each voxel, it is possible to reconstruct the trajectory of white matter pathways across the brain. This forms the basis of tractography, a technique that enables three-dimensional visualization of white matter connectivity and supports the study of large-scale brain networks.

1.3 Tractography

Fiber tractography is a three-dimensional method for reconstructing white matter pathways using diffusion MRI data. This technique is based on the analysis of the principal directions of water diffusion in white matter, which reflects the organization of axonal fiber bundles in the brain.

These principal diffusion directions estimated in each voxel can be represented using a standardized color code: fibers running from right to left appear in red, those oriented along the anteroposterior axis in green, and those oriented from inferior to superior in blue. This directional mapping facilitates the identification of major white matter tracts within the human brain.

Tractography algorithms integrate the principal diffusion directions across voxels to reconstruct global trajectories, known as streamlines. In its simplest form, this approach assumes a single dominant diffusion direction per voxel, forming a continuous vector field across the brain. Mathematically, the orientations are considered to form a three-dimensional vector field, and the trajectories are represented as parameterized curves $r(s)$ that satisfy the following differential equation [26]:

$$\frac{dr(s)}{ds} = v[r(s)]$$

where $r(s)$ defines the position along the streamline as a function of the arc length parameter s, and $v[r(s)]$ is the local direction vector at that point. The starting point r_0 is referred to as the seed point. The resulting set of streamlines is referred to as a tractogram.

However, this diffusion tensor-based approach has a major limitation: it only allows the identification of a single principal orientation per voxel. In regions where multiple fiber bundles intersect, converge, or diverge, the tensor model becomes inadequate. This can lead to errors, particularly in deterministic tractography (see section Deterministic Tractography), such as premature termination of tracking (false negatives) or deviation into unrelated adjacent tracts (false positives). To address this limitation, more advanced models have been developed in recent years. These “higher-order” approaches allow estimation of multiple fiber orientations within a single voxel without requiring prior knowledge of their number. They represent fiber orientations as a continuous function on the sphere, known as the Fiber Orientation Distribution function (FODF). An illustration comparing the tensor representation and fiber orientation distribution functions is shown in Figure 1.11, highlighting the improved ability of fiber orientation distribution functions to resolve complex fiber configurations.

Once fiber orientations have been estimated throughout the brain, the next step is to link them together to reconstruct long-range fiber tracts. This process typically begins from seed points defined within Regions of Interest (ROIs), which can be selected manually or using an atlas. This selection requires precise anatomical knowledge of white matter structures and their spatial relationships, which can

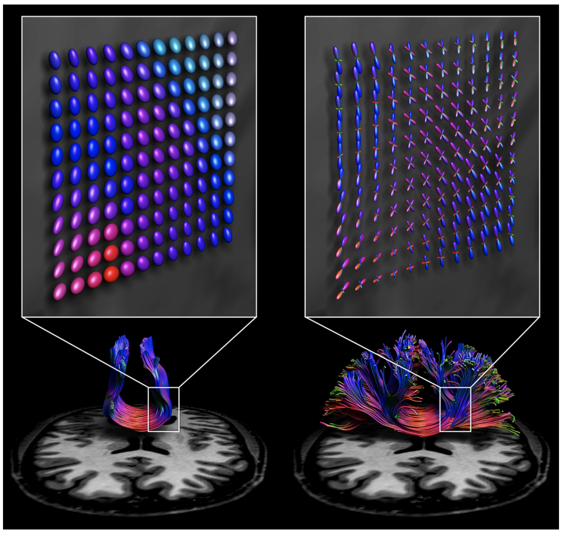

Figure 1.11: Comparison between tensor-based (left) and FODF-based (right) representations of white matter fiber orientations [26].

introduce manual delineation variability. To reduce this variability, it is also possible to use atlas-based ROIs or activation maps derived from functional imaging. An alternative method is whole-brain tractography, where tracking is initiated from numerous seed points distributed across the entire brain volume [26, 27].

1.3.1 Local versus Global Approaches

Most tractography methods, particularly streamline-based techniques, are considered local. They rely on a stepwise propagation strategy, following local fiber orientations extracted voxel by voxel, typically based on the principal eigenvector of the diffusion tensor. A well-known example is the Fiber Assignment by Continuous Tracking (FACT) algorithm [28], which uses the direction of highest diffusivity to propagate streamlines from a seed point. Local methods are fast, relatively simple to implement, and widely used. However, they have several drawbacks. The most obvious is that small errors in local orientation estimation, often due to noise or partial volume effects, can accumulate over long trajectories, leading to premature termination (false negatives) or deviation into unrelated tracts (false positives). A more fundamental limitation is that local streamline tractograms often poorly predict the actual diffusion signal measured, which questions their biological interpretability and quantitative value.

In contrast, global tractography methods aim to reconstruct all fiber paths simultaneously by optimizing a global configuration that best explains the full diffusion MRI dataset. An example is Gibbs Tracking [29], which models fibers as interacting particles in a probabilistic energy landscape. Global methods offer several advantages: they are more robust to noise and artifacts, produce more anatomically plausible tracts, and better align with the actual measured diffusion data. However, they are computationally intensive. Their use also requires precise adjustment of several parameters, and remains less common in clinical practice due to their complexity and high cost of calculation.

In summary, local approaches are fast and accessible but limited in accuracy, while global methods are more robust and data-consistent at the cost of greater computational demand and complexity [26].

1.3.2 Deterministic and Probabilistic Tracking Algorithms

While the distinction between local and global approaches focuses on the spatial scope of fiber reconstruction, tractography algorithms can also be classified based on how they handle uncertainty in orientation estimation into two types: deterministic and probabilistic.

Deterministic tracking algorithms estimate a single dominant fiber orientation per voxel and generate one trajectory from each seed point. This makes them relatively fast and computationally efficient. However, these methods have limitations. Because they rely exclusively on local orientation estimates, they are particularly vulnerable to noise, modeling inaccuracies, and errors in streamline integration. As a result, they often struggle in regions where fibers bend, cross, or merge. Additionally, deterministic tractography does not offer any indication of uncertainty in the reconstructed pathways. The outcome can also depend heavily on user-defined parameters, such as threshold values and seed placement, introducing a degree of operator dependency [15, 30].

Probabilistic tractography, by contrast, models uncertainty in fiber orientation within each voxel. From a single seed point, it generates a distribution of possible streamlines, allowing exploration of regions with complex fiber architecture or low anisotropy. As a result, this method improves sensitivity to curving and crossing fibers and provides a more biologically realistic representation of white matter pathways [15, 24]. The trade-offs of probabilistic methods include longer computation times, less intuitive visual output (expressed as probabilities or connectivity distributions), and increased risk of false positives due to overestimation of possible connections [30].

In summary, deterministic tractography is efficient and produces clearly

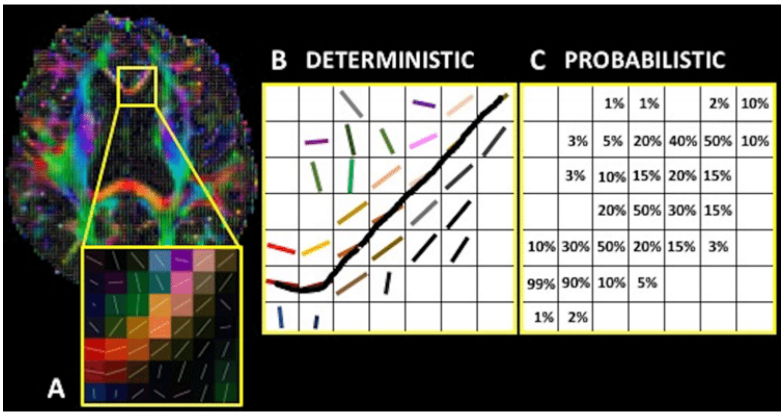

		1%	1%		2%	10%
	3%	5%	20%	40%	50%	10%
	3%	10%	15%	20%	15%	
		20%	50%	30%	15%	
10%	30%	50%	20%	15%	3%	
99%	90%	10%	5%			
1%	2%					

Figure 1.12: Different Tractography Algorithms. A: Level of anisotropy. B: Deterministic fiber tracking; the path of the fiber through voxels is deduced from one diffusion orientation for every voxel. C: Probabilistic fiber tracking; tractography created from a probability distribution of diffusion directions in each voxel [31].

defined tracts, but may miss or misrepresent complex fiber configurations. Probabilistic tractography offers more comprehensive modeling of uncertainty and fiber complexity, at the cost of longer processing time and reduced specificity. Figure 1.12 illustrates the difference between these two approaches.

While tractography focuses on reconstructing white matter pathways, tractometry builds upon these reconstructions to quantitatively assess their microstructural properties. The following section introduces tractometry as a framework for extracting biologically relevant information from diffusion-derived tracts.

1.3.3 Tractometry

Tractometry is an analysis framework that involves the identification of major white matter tracts in individual subjects and the quantitative evaluation of their microstructural properties [32]. By combining tractography with DWI, tractometry enables the measurement of tissue characteristics along the trajectories of reconstructed fiber bundles.

This approach typically involves computing diffusion-derived metrics, such as FA, MD, AD and RD at multiple points along each tract. These measures provide biologically relevant information on axonal density, myelination, and tissue integrity, and can be used to generate tract profiles that capture spatial variations in microstructure [33].

Tractometry is particularly valuable for group comparisons between clinical populations and healthy controls. It allows researchers to identify tract-specific alterations associated with various neurological conditions, including neurodegenerative diseases, brain injuries, and neurodevelopmental disorders. This makes tractometry a promising tool for discovering imaging biomarkers and understanding disease progression [33].

Moreover, tractometry helps capture the downstream impact of localized lesions or degeneration on structurally connected pathways. However, the technique remains limited by factors such as the spatial resolution of diffusion imaging, signal-to-noise ratio (SNR), and potential inaccuracies in tract reconstruction [32].

In order to interpret the clinical relevance of tract profiles, it is important to understand the biological meaning of each diffusion metric. The diffusion-derived metrics used in tractometry each reflect distinct microstructural aspects of white matter. FA quantifies the directionality of water diffusion and is commonly interpreted as a global index of white matter integrity. Higher FA values are generally reflecting more coherent and well-myelinated fiber bundles [13, 34]. MD represents the average magnitude of diffusion and increases in MD are typically associated with tissue damage, greater extracellular space, or demyelination [35]. AD, the principal eigenvalue of the diffusion tensor, reflects diffusion along axonal fibers and is considered a marker of axonal integrity. A reductions in AD may indicate axonal injury or loss [34]. Finally, RD, which captures diffusion perpendicular to the main axis, is sensitive to myelin integrity. An elevated RD is suggesting demyelination or alterations in axonal diameter [13, 35].
Taken together, these metrics allow for a nuanced interpretation of white matter microstructure: for instance, a pattern of high FA coupled with low MD and RD is often considered indicative of good white matter integrity [35]. These interpretations are essential when assessing the relationship between tract microstructure and clinical outcomes.

In this study, tractometry was applied to a specific set of white matter pathways known to be involved in auditory and cognitive processing. The following section describes the anatomical and functional relevance of the selected tracts, which were delineated and analyzed using the framework introduced above.

1.4 Tracts Analyzed in This Study

White matter tracts serve as essential pathways for transmitting neural signals between different cortical regions. It is through these connections that complex

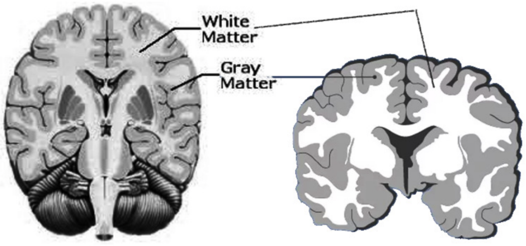

Figure 1.13: Anatomical illustration showing the distribution of grey matter (dark grey) and white matter (white) [36].

cognitive and sensory functions are organized [15]. White and grey matter play distinct but complementary roles in the central nervous system. Grey matter, composed primarily of neuronal cell bodies, is responsible for processing and integrating information, and forms the outer layer of the brain (the cortex) as well as the central core of the spinal cord [36]. In contrast, white matter contains bundles of myelinated axons that facilitate the rapid transmission of electrical signals between grey matter regions, thus enabling efficient communication across the brain. The difference between the grey and white matter is represented on Figure 1.13.

In this thesis, four specific tracts were selected for analysis: the Arcuate Fasciculus (AF), the Uncinate Fasciculus (UF), the Inferior Fronto-Occipital Fasciculus (IFOF) and tracts running through the Corpus Callosum (CC).

1.4.1 Arcuate Fasciculus

The AF is a major white matter tract of the brain, historically considered one of the pillars of the language network. It connects frontal and temporal regions, in particular the Broca's and Wernicke's areas, through a curved path that loops around the Sylvian fissure [15].

Anatomically, the arcuate fasciculus is generally subdivided into three segments: a long segment, which directly connects the inferior frontal gyrus (Broca's area) to the middle and superior temporal gyrus (Wernicke's area); an anterior segment, linking frontal regions to inferior parietal gyrus; and a posterior segment, connecting these parietal regions to the superior and middle temporal areas [15, 37].

The long branch is classically involved in phonological processing, whereas the anterior and posterior segments appear to be more involved in semantic processing and lexical memory tasks. In the left hemisphere, which is typically dominant for language, the AF plays a crucial role in verbal comprehension and production, auditory repetition, reading, and verbal fluency [18]. In the right hemisphere, although its role is less central, the arcuate fasciculus appears to be involved in prosodic, visuospatial, and semantic aspects of language [15].

Recent work, notably by Ivanova et al. (2016), has highlighted specific links between the fasciculus segments and certain language functions. Alterations in the posterior segment are associated with comprehension deficits, while lesions in the anterior segment mainly affect verbal production [18].

1.4.2 Inferior Fronto-Occipital Fasciculus

The inferior fronto-occipital fasciculus is an association tract that connects posterior occipital regions to the frontal lobes. It passes through the temporal lobe, running medially to the Inferior Longitudinal Fasciculus (ILF), and projects to the inferior and middle orbitofrontal cortex.

It has been suggested that the IFOF is involved in visual object discrimination, by connecting dorsomedial occipital and parietal regions to the posterior prefrontal cortex. Its frontal connections, particularly with the inferior frontal gyrus, are also involved in executive functions related to semantic processing [38].

A functional MRI study conducted on patients with schizophrenia showed a correlation between reduced integrity of the left IFOF and impairments in verbal memory, visual memory, and processing speed [15]. Moreover, direct evidence from intraoperative stimulation in patients with right-hemispheric gliomas has revealed that the right IFOF is critically involved in non-verbal semantic processing [39]. Finally, direct stimulation of the IFOF may lead to anomia[1] without inducing visual disturbances, suggesting a specific role in lexical access [18].

1.4.3 Uncinate Fasciculus

The UF is a short, bilateral white matter association tract connecting the anterior temporal lobe to the orbitofrontal cortex passing through the ventral portion of the external capsule. As part of the limbic system, it plays a central role in

---

[1] Anomia corresponds to an alteration in the ability to retrieve words spontaneously, often reflecting a disturbance in their access or mental representation. [40].

interactions between memory, emotion, and decision-making [41, 42].

It has been suggested that the UF is strongly involved in various language functions, including comprehension, production, lexical-semantic retrieval and control, as well as reading, semantic and phonemic verbal fluency, and the naming of proper nouns. A study involving 129 brain-lesioned patients showed that its alteration is associated with reduced performance in retrieving the names of famous people, highlighting its role in face-name identification [15].

Degeneration of this tract has been observed in neurodegenerative disorders such as primary progressive aphasia and semantic dementia, although its precise role in specific language functions remains to be clarified [18].

On the affective and social level, the UF is thought to serve as a critical communication pathway between the amygdala, hippocampus, and orbitofrontal cortex. It may contribute to reward evaluation and behavioral adaptation. As a link between memories associated with a person and the emotions they elicit, damage to this tract could contribute to psychiatric disorders affecting emotions, social interactions, and decision-making [41, 43].

1.4.4 Corpus Callosum

The CC is the largest white matter structure in the brain, ensuring communication between the cerebral hemispheres. It plays a central role in the integration and transfer of sensory, motor, and higher cognitive information [44].

This structure is not homogeneous, but is composed of several functionally distinct subregions. The genu, its most anterior part, connects the prefrontal cortices. The anterior and posterior midbody portions connect the motor and somatosensory areas of both hemispheres. More caudally, the isthmus and splenium, which form the posterior third of the corpus callosum, establish connections with the temporal, parietal, and occipital regions. The splenium, in particular, connects the dorsal parietal areas and visual regions of the occipital lobes [17].

The anterior callosal fibers are primarily involved in transferring motor information between the frontal lobes, whereas the posterior fibers participate in the transmission of somatosensory, auditory, and visual signals, respectively in the midbody, isthmus, and splenium [45].

Chapter 2

Deafness

Understanding the structural and functional organization of the brain is essential for exploring sensory deficits such as deafness. After reviewing the principles of MRI and diffusion imaging techniques, which allow the visualization of white matter connectivity, this chapter will now focus on the auditory system and how impairments within this system can lead to hearing loss.
This chapter provides an overview of the auditory system, including the anatomy of the human ear, the ascending auditory pathways, and the auditory cortex. The various forms of deafness are then presented, along with cochlear implants as a treatment option, and the principles of audiometric evaluation.

2.1 Auditory System

2.1.1 Human Ear Anatomy and Auditory Transduction Mechanism

The auditory system begins with the ear, which can be divided into three parts: the outer, middle, and inner ear. The role of the outer and middle ear is to amplify mechanical resonance in order to transmit optimal vibrations to the inner ear. The outer ear includes the auricle (or pinna), which helps amplify sound, and the external auditory canal. Continuously connected to the external canal, the middle ear contains the tympanic membrane and the ossicles. These ossicles serve as an impedance adapter between the middle and inner ear. Finally, the inner ear consists of the cochlear nerve, the cochlea, and the organ of Corti, which contains the sensory hair cells responsible for sound transduction (see Figure 2.1).

The auditory transduction process begins when air pressure oscillations, collected by the auricle of the outer ear, are transmitted through the external

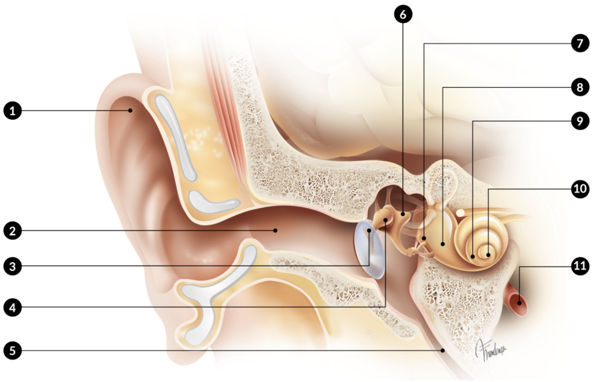

Figure 2.1: Schematic representation of the human ear anatomy. (1) Auricle (2) External Auditory Canal (3) Tympanic Membrane (4) Malleus (5) Eustachian Tube (6) Incus (7) Stapes (8) Superior Semicircular Canal (9) Cochlea (10) Apex (11) Carotid Artery [46].

auditory canal to the tympanic membrane. The tympanic membrane, set into vibration like a drumhead, transmits these vibrations through the ossicles of the middle ear, which are set into motion in sequence. The final ossicle, connected to the cochlea at the oval window, the interface between the middle and inner ear, transmits the vibrations into the cochlea.
Inside the cochlea, movement of the oval window sets the fluid in the vestibular duct (perilymph) into motion. This fluid communicates at the apex of the cochlea with the perilymph in the tympanic duct, which is also set into motion. This mechanism in turn causes vibration of the round window at the base of the cochlea, which leads to movement of the basilar membrane. This vibratory motion causes shearing of the hair cell stereocilia, resulting in the transduction of sound, that is, its conversion into an electrical signal through changes in the cell membrane potential (see Figure 2.2).

This movement of the basilar membrane is not uniform along its entire length: it depends on the frequency of the incoming sound. This organization, known as cochlear tonotopy, allows the cochlea to decompose complex sounds into pure frequency components. Tonotopy refers to the spatial organization of neuronal populations based on their preferred frequency response. Low-frequency sounds induce vibrations at the apex of the cochlea, while high-frequency sounds primarily vibrate the basal portion of the basilar membrane.

Once the mechanical vibrations are converted into electrical signals by the inner hair cells, these signals are transmitted through the auditory pathways initiating

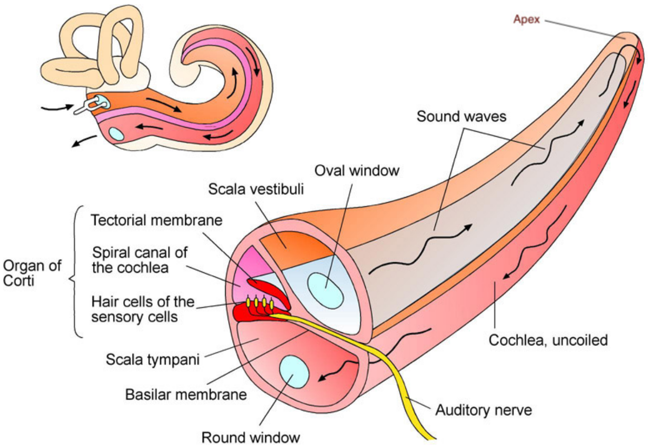

Figure 2.2: Schematic representation of the human cochlea (uncoiled view), showing the propagation of sound waves through the scala vestibuli and tympani, and the activation of hair cells in the organ of Corti located on the basilar membrane [47].

central auditory processing.

2.1.2 Ascending Auditory Pathways

Auditory signals, once transduced in the cochlea, are transmitted to the auditory cortex via a series of relay stations in the brainstem and midbrain. These ascending pathways preserve the tonotopic organization of the cochlea and allow rapid and bilateral processing of auditory information.

The inner hair cells of the organ of Corti are connected to neurons of the spiral ganglion. Initially, signals propagate along the cochlear nerve to the cochlear nuclei located in the brainstem on the ipsilateral side. Most auditory information crosses the midline. However, each cerebral hemisphere processes stimuli from both the ipsilateral and contralateral sides. This organization presents advantages such as, in the event of a lesion in one hemisphere, hearing is only minimally affected.

The first stop of the auditory signal is the cochlear nucleus. From there, most neurons cross to the contralateral side. This constitutes the main route taken by auditory information. However, a secondary pathway exists, in which some neurons remain on the ipsilateral side. In both cases, the neurons synapse at the level of the superior olivary complex, also located in the brainstem. The superior olivary complex plays a key role in sound localization through coincidence-detecting neurons.

Next, the signal continues its course along the lateral lemniscus to reach the inferior colliculus in the midbrain. From the inferior colliculus, information is relayed to the medial geniculate nucleus of the thalamus. Most neurons in this pathway remain ipsilateral, although some still cross to the opposite hemisphere. Finally, the auditory information reaches the auditory cortex.

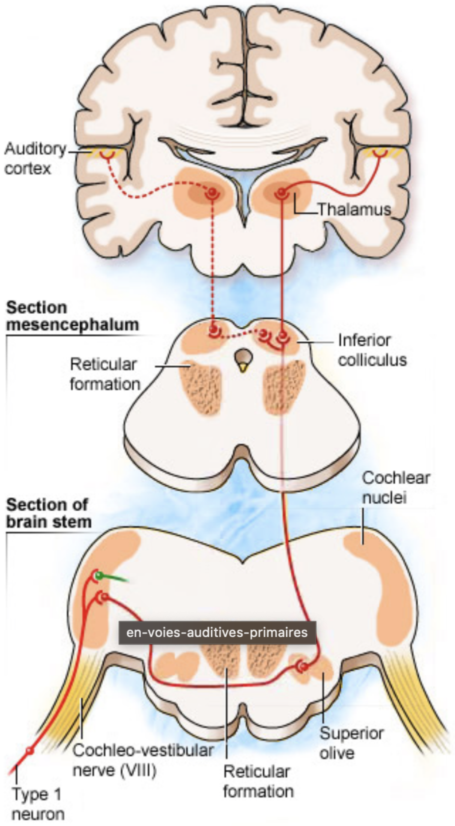

Figure 2.3: Schematic representation of the ascending auditory pathways. These travel through the brainstem via successive relays: cochlear nucleus, superior olivary complex, lateral lemniscus, and inferior colliculus. The signal then passes through the thalamus (medial geniculate body) and projects to the superolateral region of the temporal lobe (primary auditory cortex), before spreading to the secondary and associative auditory cortices [48, 49].

2.1.3 Auditory Cortex

The Auditory Cortex (A1) and the secondary auditory areas are located within the Sylvian fissure and occupy the Temporal Superior Gyrus (STG). The primary auditory area shows significant interindividual variability, both in volume and in precise location. The primary auditory cortex exhibits a tonotopic organization, similar to the cochlea, with bilateral, but predominantly contralateral, representation of acoustic stimuli. The secondary auditory areas correspond to Brodmann area 52, which is located anterior to the primary auditory cortex (see Figure 2.4) [48]. These areas are involved in more complex auditory processing, including the integration of temporal and spectral features and early stages of speech perception.

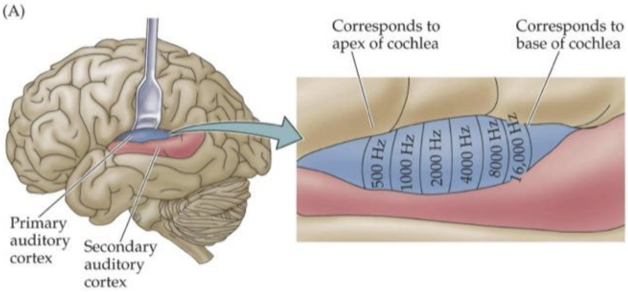

Figure 2.4: Auditory Cortex. (A) and (B) The primary auditory cortex A1 is shown in blue, and the surrounding auditory belt areas are shown in red [50].

Understanding the organization and function of the auditory system provides a foundation for exploring what happens when this system is disrupted. The following section presents the main forms of hearing loss and their underlying causes.

2.2 Deafness

Hearing loss, or deafness, refers to a partial or total inability to perceive sound. In humans, the audible frequency range spans from 20 to 20,000 Hz, with speech comprehension mainly occurring between 100 and 3500 Hz. Disruption of hearing within this critical range can significantly impact communication and quality of life.

There are four types of hearing loss [51]:

1. Conductive hearing loss. This type of hearing loss occurs when there is a physical obstruction preventing sound from reaching the inner ear through the outer or middle ear. It can often be treated with medication or surgery.

2. Sensorineural hearing loss. This type of hearing loss arises when the function of the inner ear or the auditory nerve is impaired. It is usually due to irreversible damage to the hair cells, which are not capable of regenerating.

Causes include acoustic trauma leading to hair cell destruction, exposure to ototoxic substances, inner ear infections such as mumps or meningitis, or presbycusis, an age-related, progressive decline in hearing, especially affecting high frequencies [52].

3. Mixed hearing loss. This type of hearing loss involves a combination of both conductive and sensorineural components.

4. Auditory neuropathy spectrum disorder. In this condition, sound enters the ear normally, but due to damage to the inner ear or auditory nerve, the signal is not transmitted in a coherent manner to the brain, making sound processing difficult.

In addition to anatomical classification, hearing loss can also be described based on the timing of onset. Prelingual hearing loss occurs before the development of language, while postlingual (or acquired) hearing loss develops after language acquisition.
Different forms and degrees of hearing loss also exist. Figure 2.5 presents a commonly used classification scheme.

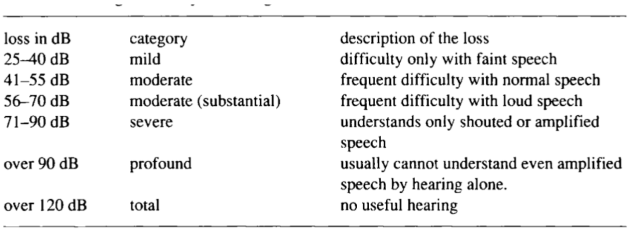

loss in dB	category	description of the loss
25–40 dB	mild	difficulty only with faint speech
41–55 dB	moderate	frequent difficulty with normal speech
56–70 dB	moderate (substantial)	frequent difficulty with loud speech
71–90 dB	severe	understands only shouted or amplified speech
over 90 dB	profound	usually cannot understand even amplified speech by hearing alone.
over 120 dB	total	no useful hearing

Figure 2.5: A Summary of Hearing Losses [52].

In the context of this thesis, the focus will be on postlingual sensorineural hearing loss. Postlingual sensorineural hearing loss is primarily caused by irreversible damage to the cochlea, particularly the hair cells. When this transduction mechanism is compromised, an alternative solution is to directly stimulate the auditory nerve. This is the fundamental principle behind cochlear implantation.

2.3 Cochlear Implant

In normal hearing, sound is transmitted from the outer ear to the cochlea via the middle ear, where it is converted into electrical impulses that the brain can interpret. In most cases of severe hearing loss, this conversion process within the cochlea is impaired. A cochlear implant bypasses the natural conversion process by directly stimulating the auditory nerve with electrical impulses. Therefore, the cochlear implant must replicate and replace the auditory functions normally carried out by the outer, middle, and inner ear.

A cochlear implant is a medical device that restores hearing in individuals with severe to profound deafness. It consists of two components: an internal part, surgically implanted, and an external part, worn behind the ear.

The external component includes a microphone, which captures environmental sounds, and a speech processor, which analyzes and converts these sounds into digital signals adapted to the individual's level of hearing loss. This information is then sent to a headpiece equipped with a transmitter, which relays the signal to the internal implant.
The internal component consists of an array of 12 to 22 electrodes implanted along the cochlea, usually covering the first one and a half turns, over a length of approximately 2 cm. These electrodes are connected to one or more internal current sources and are activated based on instructions received from the external device. Once the signal is received, the implant converts it into electrical impulses, which are transmitted via a wire to the electrode array. An illustration of the cochlear implant is represented on the Figure 2.6.

Cochlear implants take advantage of the tonotopic organization of the cochlea: each electrode contact is positioned near auditory nerve fibers responsible for encoding different sound frequencies. When an electrode is stimulated, it generates an auditory perception generally corresponding to its location. Thus, the auditory nerve is directly stimulated, allowing the brain to interpret these electrical impulses as sound information [53, 54].

To ensure optimal auditory outcomes, cochlear implants must be carefully calibrated to each patient's individual hearing profile. This process relies on the results of various audiometric assessments. Audiometry is therefore essential not only for diagnosing hearing loss but also for monitoring and adjusting the implant's performance over time.

2.4 Audiometry

There are several types of audiometric tests, including pure-tone audiometry and speech audiometry, which are non-invasive and painless. Pure-tone audiometry measures the hearing threshold, i.e., the minimum intensity at which a patient perceives a sound, across different tested frequencies. This test is performed in a

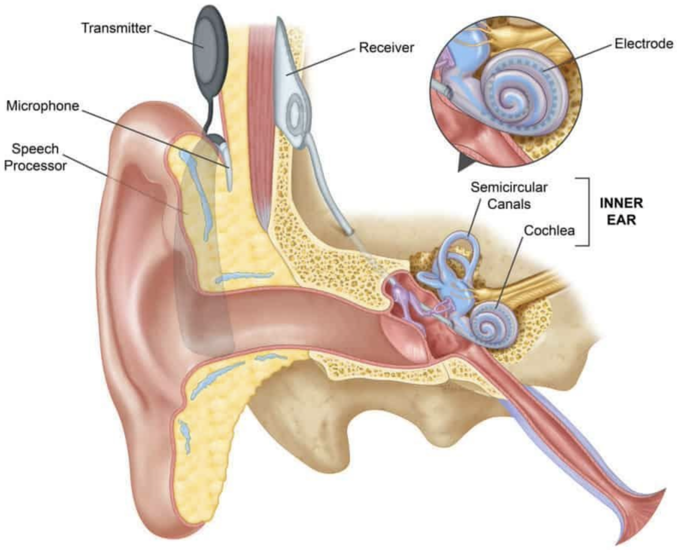

Figure 2.6: Anatomical illustration of a cochlear implant, showing both external components (microphone, speech processor, transmitter) and internal components (receiver and electrode array inserted into the cochlea) [55].

soundproof booth and involves the presentation of pure tones. Speech audiometry, on the other hand, assesses the patient's ability to understand words at various sound intensities. It is also conducted in a soundproof environment. During the evaluation, sequences of one- or two-syllable words or phonemes are presented at different frequencies, and the patient is asked to repeat them [56].

The Deggouj-Wathour (DEWA) test evaluates audiovisual integration. Its goal is to analyze speech comprehension and guide speech therapy strategies based on auditory, visual, or combined stimuli. It assesses the extent to which a deaf or hard-of-hearing individual can enhance oral comprehension by relying on auditory cues, visual cues (lip reading), and their interaction. The test involves repeating lists of words presented under different experimental conditions isolating auditory and/or visual modalities. To avoid the influence of mental guessing, only lists of monosyllabic words are used. These words, exclusively common nouns, are selected based on the phoneme frequency in the French language [54].

The Average Word Recognition Score (AWRS) is a metric used in speech audiometry tests to assess overall word comprehension. AWRS is a test demonstrating the ability of a patient to understand and repeat words. The final score corresponds to the percentage of words correctly repeated [57].

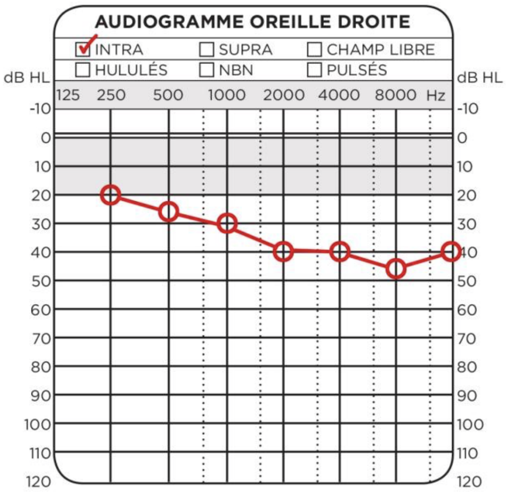

Figure 2.7: Example of audiogram for the right ear. The grey part representing a normal hearing [59].

The results of auditory tests, whether tonal or speech-based, are typically represented using a speech audiogram, in which sound pitch (as a function of frequency) and intensity (measured in decibels) are plotted. An example of an audiogram is represented on Figure 2.7 [58, 59].

2.5 Previous Studies

Several recent studies have investigated the cerebral mechanisms associated with deafness and their influence on outcomes after cochlear implantation. This section reviews current findings related to white matter changes and brain plasticity, with particular attention to their potential predictive value. The literature is structured thematically to highlight key observations and clinical implications.

2.5.1 Literature Review on White Matter Microstructure, Deafness, and Cochlear Implant Outcomes

1. Language-related white matter tracts show segmental functional specialization, supporting sub-tract analysis. The traditional view of white matter language pathways, particularly the AF, as functionally homogeneous structures is increasingly challenged by diffusion imaging studies. Anatomically segmented analyses reveal distinct functional roles along different portions of a given tract.

Ivanova et al. (2016), in a study involving post-stroke aphasic patients, demonstrated that different portions of the left AF have distinct functions: the temporal segment is involved in both language comprehension and production, while the parietal segment supports production. Additionally, the left IFOF, particularly its middle and inferior temporal portions, was associated with comprehension. These findings challenge the notion that tracts can be treated as uniform functional units [18].
Similarly, Catani et al. (2005) revised the classical model of fronto-temporo-parietal connectivity based on tractography in healthy subjects. They identified a direct segment of the left AF linking Broca's and Wernicke's areas, which supports rapid phonological processing, and an indirect segment passing through the inferior parietal cortex (Geschwind's territory), which is thought to support semantic processing [37].
Ivanova et al. (2021) further supported this model by investigating the segmental contributions of the AF to verbal repetition in aphasic patients. They found that the long segment was strongly associated with repetition of pseudowords, while the posterior segment was linked to word repetition, suggesting a role in lexical access. The anterior segment, by contrast, showed no significant association. These findings underscore the functional dissociation across AF segments and reinforce the relevance of tract segmentation [60].
Teubner-Rhodes et al. (2016), using a node-wise approach in healthy adults, further demonstrated functional variation within the AF. The left posterior temporal segment was positively correlated with vocabulary scores, independently of the age of the subjects. In contrast, cognitive processing speed was associated with MD in the left anterior and medial AF and in the right medial and posterior AF, with age-dependent modulation [61].
Finally, Chang et al. (2012), studying prelingually deaf children, provided indirect support for localized microstructural analysis. Using a voxel-wise approach, they found that better cochlear implant responders exhibited higher FA in the left Broca's area and the genu of the corpus callosum. These values were strongly correlated with word recognition and sentence comprehension scores [62].
Roux et al. (2021) provided further evidence of sub-tract specialization by showing that different portions of the right IFOF support distinct cognitive functions. Using direct electrostimulation and tractography in awake patients, they found that ventral streamlines were associated with visual semantic processing, while dorsal streamlines were involved in mentalizing. This functional dissociation reinforces the relevance of cluster-level analyses when investigating white matter tracts [63].

Collectively, these studies support the need to investigate white matter tracts segmentally rather than as whole structures, a rationale that supports the cluster-based tract analysis used in the present study.

2. Auditory deprivation leads to durable microstructural alterations, particularly in auditory and associative regions. Diffusion MRI studies have shown that deafness, especially when early or prolonged, results in microstructural changes in white matter. These changes are seen in the STG, IFOF, CC, and UF and include reduced FA and increased RD, suggesting demyelination.

Li et al. (2012) compared hearing controls with congenital and early-acquired deaf individuals. They reported significant FA reductions in the right STG, left Heschl's gyrus (among congenital cases), and the splenium of the CC. These alterations were primarily driven by increased RD, indicating demyelination. In early-acquired deafness, FA was negatively correlated with age of onset but not duration, supporting a critical period hypothesis for auditory white matter development [64].
Huang et al. (2024), studying individuals with noise-induced hearing loss, found reduced FA and increased RD, MD, and AD in the left IFOF and right external capsule. These changes were correlated with hearing loss severity and anxiety scores, highlighting a multisystemic impact of auditory deprivation [65].
Luan et al. (2019) confirmed these IFOF-related changes bilaterally. FA in the IFOF, particularly near the STG, was negatively correlated with hearing thresholds, suggesting a degradation of connectivity due to disuse. The authors emphasized the IFOF's role in audiovisual integration and semantic processing [66].
Finally, Armstrong et al. (2020) reported increased MD in the left IFOF and body of the CC, and decreased FA in the bilateral UF. These changes were more pronounced in participants with poorer hearing, suggesting that both semantic and interhemispheric pathways are affected in hearing loss [67].

Together, these studies indicate that auditory deprivation leads to widespread, durable alterations in the microstructure of white matter tracts crucial for language and auditory processing.

3. White matter integrity has emerged as a promising predictor of cochlear implant outcomes. Several studies suggest that diffusion metrics, particularly FA and RD, may serve as pre-operative biomarkers of post-implantation auditory performance.

As mentioned earlier, Chang et al. (2012) found that higher FA in the left Broca's area, genu of the CC, and medial geniculate body was strongly correlated with improved CAP scores, word recognition, and sentence comprehension [62]. This direct link between structural integrity and functional outcome supports the use of such measures in clinical prediction.
Quatre et al. (2024), in a systematic review of diffusion imaging studies, reported consistent reductions in FA, and increases in RD in deaf individuals, particularly in the superior temporal cortex (anterior and posterior), Heschl's gyrus, splenium, and both the body and genu of the corpus callosum. These effects were most pronounced in congenital deafness, though also present in some postlingual cases. The authors conclude that FA is currently the most robust imaging-derived candidate for predicting CI outcomes, even though no clinically validated threshold has yet been established [68].

Critical conclusion Recent studies underscore the importance of white matter microstructure in auditory and language-related regions, both for understanding the effects of deafness and for anticipating outcomes after cochlear implantation. However, several limitations remain in the current literature.

First, most studies treat white matter tracts as single units, neglecting their internal functional heterogeneity. Yet robust findings from stroke, functional connectivity, and microstructural research show that different tract segments may subserve distinct functions. This justifies the use of segmented or cluster-based tract analyses, as employed in the present study.

Second, although FA is the most widely used diffusion metric, the others, such as RD, MD, and AD, are more specific to certain neural processes like demyelination or axonal damage. These are rarely analyzed in detail and sould be incorporated for more precise interpretation.

Finally, most studies focus on congenital or prelingual deafness. Postlingually deaf individuals, who represent a large portion of adult CI candidates, remain underrepresented in research. This limits the generalizability of current findings to real-world clinical populations.

Part II

Analysis for biomarkers of success of the Cochlear Implant

Motivation and previous findings

This study builds upon previous work by Anaïs Grégoire, who identified brain regions predictive of cochlear implant outcomes using diffusion-weighted MRI. In her analysis, correlations between behavioural performance and diffusion metrics were conducted using a whole-brain voxel-wise approach. This method allowed the detection of clusters where FA was significantly associated with behavioural outcomes at six months post-implantation.

Specifically, one cluster was correlated with AWRS scores, shown in Figure 2.8 and four clusters were associated with DEWA scores, shown in Figure 2.9. These findings provided insights into the brain regions potentially involved in cochlear implant success. However, the whole-brain voxel-wise strategy does not explicitly link the findings to specific anatomical white matter tracts.

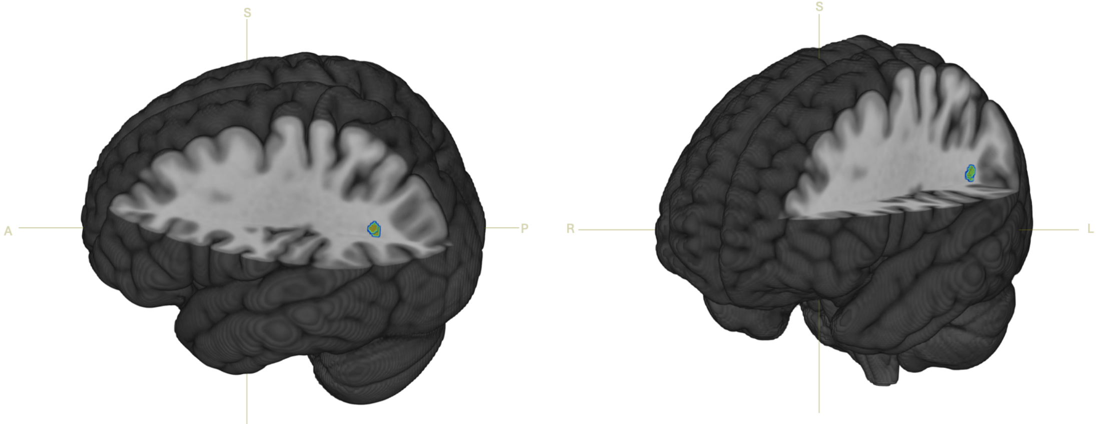

Figure 2.8: The cluster identified in whole-brain voxel-wise analysis by Dr. Anaïs Grégoire, significantly correlated with AWRS score at 6 months post-implantation.

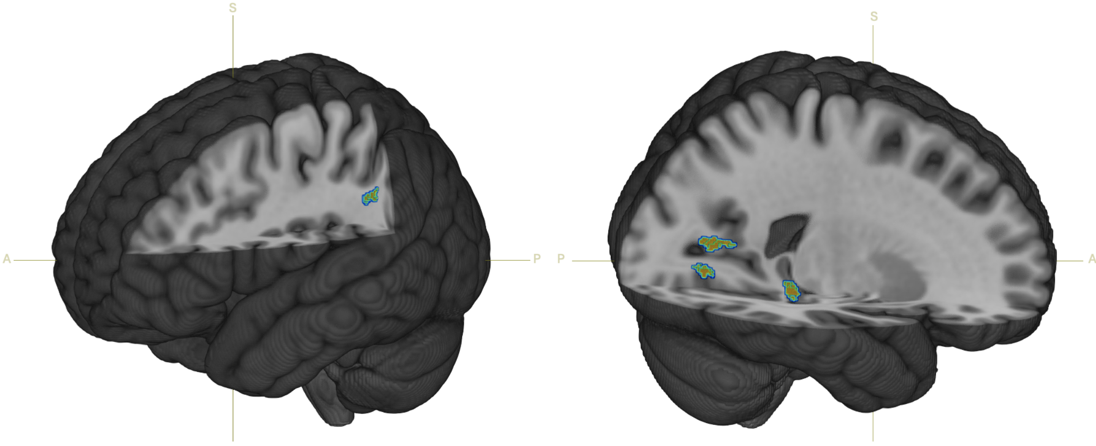

Figure 2.9: Clusters identified in the voxe-wise analysis by Dr. Anaïs Grégoire, showing significant correlation with DEWA scores.

The aim of the present study is therefore to build upon these results by adopting a tractography-based approach, focusing on known white matter fascicles. This method aims to validate and refine previous observations with greater anatomical specificity, by assessing diffusion metrics within targeted tracts and correlating them with post-operative behavioural outcomes. The selection of tracts investigated in this study was guided by the anatomical locations of the clusters identified as significant in the previous whole-brain analysis.

Chapter 3

Materials and Methods

This section provides a detailed description of the study participants, the behavioural and imaging data collected, the preprocessing steps applied to the diffusion-weighted MRI data, and the tractography and statistical analyses performed. The methodological workflow is summarized in Figure 3.1.

3.1 Participants

This study included 65 participants (mean age = 57.95 years; range = 17–88 years) with acquired hearing loss who underwent cochlear implantation. Among them, 36 were women and 29 were men. Handedness data showed 55 right-handed, 7 left-handed, and 3 ambidextrous individuals. All participants underwent pre-operative MRI and pre- and post-operative audiometric evaluation.

Two participants passed away within one year following implantation, which explains the absence of 12-month audiometric data for these individuals. These cases were excluded from statistical analyses involving one-year outcome measures.

3.2 Behavioural Data

Audiometric data were collected for all participants by Dr. Anaïs Grégoire as part of a previous study. Two standardized speech perception tests were administered: the AWRS and the DEWA audiovisual tests (see Section 2.4 for details.). These tests were conducted at three time points: pre-operatively, and at 6 and 12 months post-operatively. Pre-operative AWRS scores were obtained both with and without hearing aids, while the DEWA test was conducted with hearing aids only. All scores were normalized to a scale from 0 to 1. In addition to test performance, the duration of hearing aid use prior to cochlear implantation was recorded for each

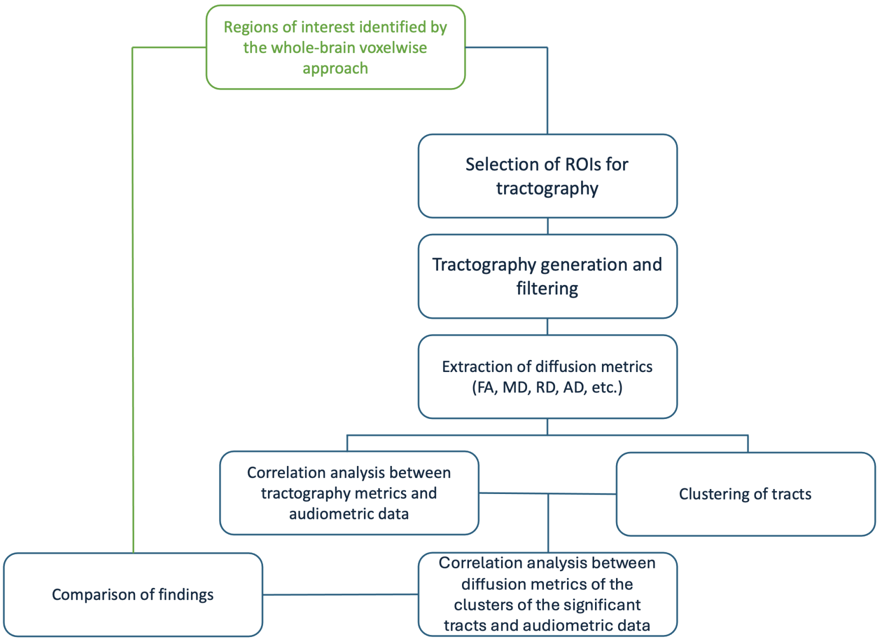

Figure 3.1: Schematic representation of the key steps of this thesis. In green: previous findings obtained by Dr. Anaïs Grégoire; in blue: method developed in the current study.

participant. The distributions of participant age and hearing aid use duration are provided in Appendix A. All behavioural data were compiled into a single Excel table, with one row per patient and columns corresponding to each test score and clinical variable.
To better illustrate the interindividual variability in the evolution of auditory performance following cochlear implantation, the Figure 3.2 shows the progression of AWRS and DEWA scores for each patient at three evaluation time points: pre-operative, 6 months post-operative, and 12 months post-operative.

In addition to behavioural scores, all participants also underwent pre-operative anatomical and diffusion-weighted MRI scanning, which was used for subsequent neuroimaging analyses.

3.3 MRI Acquisition

MRI data used in this study were provided by Saint-Luc Hospital in Brussels. Two modalities of MRI data were used: anatomical and diffusion-weighted images. Anatomical images consisted of T_1-weighted volumes with a resolution of 256x256x224 voxels, a voxel size of 0.976x0.976x1.0 mm^3, and a TE of 4.92 ms.

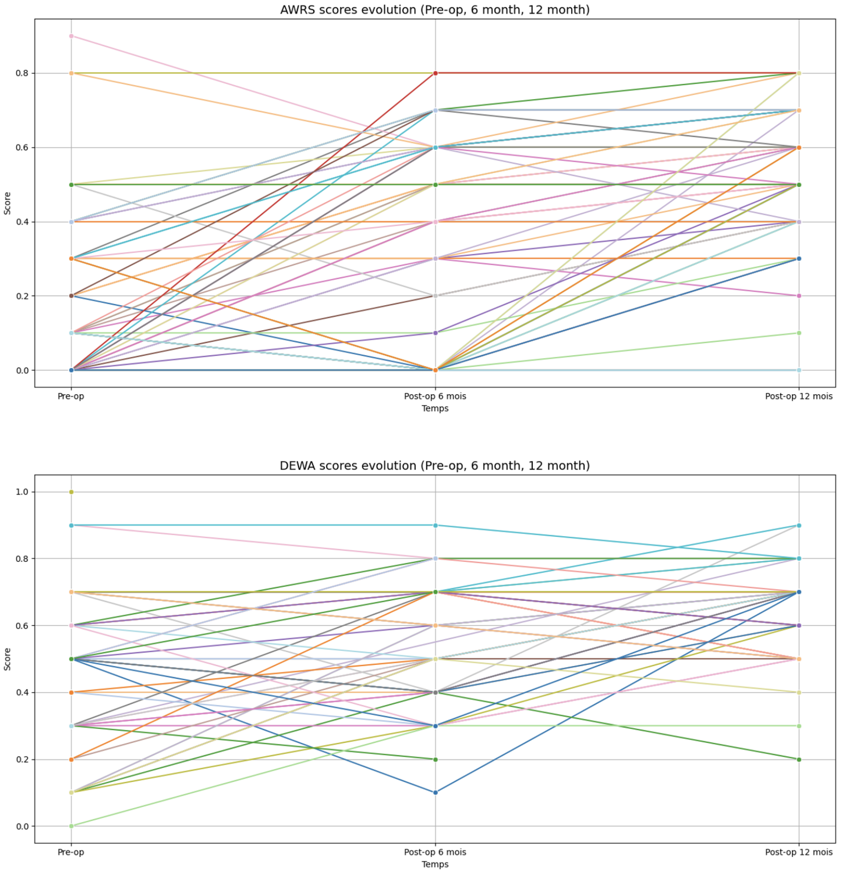

Figure 3.2: Individual evolution of audiometric scores for AWRS and DEWA over time (pre-operative, 6 months post-operative, and 12 months post-operative). Each line represents one patient, displayed in a unique color. These plots highlight the diversity of auditory recovery trajectories across the study population.

Diffusion-weighted images were acquired with a resolution of 128x128x56x65, a voxel size of 1.953x1.953x2.0 mm^3, a TE of 74 ms, and a TR of 9000 ms. A total of 65 volumes were acquired, including one $b = 0$ s/mm^2 volume and 64 diffusion-weighted volumes with a b-value of 800 s/mm^2. As only a single non-zero b-value was used, the acquisition is considered single-shell.

3.4 Preprocessing

As discussed in the Limitations and Artifacts section, diffusion MRI data are prone to various artifacts and distortions which can significantly affect the accuracy of diffusion measures and downstream analyses. Therefore, an essential preprocessing step is required to mitigate these imperfections and to improve the reliability of diffusion metrics. In this study, the `Elikopy` library was employed to preprocess the diffusion-weighted MRI data. The Elikopy library provides a standardized, reproducible framework for processing large datasets and integrates several correction steps commonly used in diffusion MRI preprocessing pipelines [69, 70].

During the preprocessing of diffusion images, several corrections were applied to improve the quality of the raw data. First, brain extraction, skull stripping, was performed to isolate cerebral tissue from extracranial structures. The images were then resampled to an isotropic resolution of 2x2x2 mm^3 to correct for interpolation artifacts introduced during clinical acquisition. Denoising was carried out using the MPPCA (Marchenko–Pastur Principal Component Analysis) method [71], allowing for a reduction of thermal noise, specifically Rician noise, without introducing artifacts or excessive smoothing. Corrections for eddy current were also applied using the Eddy algorithm [20] from FSL(FMRIB Software Library) [21, 22]. In addition, susceptibility-induced distortions were corrected using the Topup tool [72]. In the absence of data acquired with multiple phase-encoding directions, the deformation field was estimated from the T_1-weighted image. A detailed summary of the preprocessing pipeline, including the tools used and their corresponding objectives, is provided in Appendix B.

3.4.1 Diffusion Modeling

Regarding diffusion modeling, the DTI model was implemented. This approach allows the estimation of key microstructural metrics such as FA, RD, AD and MD, which are widely used to characterize white matter microstructure.
Although the Neurite Orientation Dispersion and Density Imaging (NODDI) model was also implemented and yielded additional microstructural parameters such as the intra-cellular volume fraction (ICVF) and orientation dispersion index (ODI),

these data were not used in the present study.

3.5 Tractography and ROIs

The selection of white matter tracts investigated in this study was guided by prior work conducted by Dr. Anaïs Grégoire. Based on these findings, the present work focused on bilateral AF (divided into anterior, posterior, and long segments), the IFOF, the UF, and five subdivisions of the CC.
Unless otherwise specified, the following abbreviations are used throughout the figures: R = right, L = left, A = anterior, P = posterior, S = superior.

3.5.1 Regions of Interest

Two types of ROIs were used in this study. Some were extracted from the Automated Anatomical Labeling (AAL) atlas [73] and defined in Montreal Neurological Institute (MNI) space [74], MNI152, using MRtrix3 tools [75], while others were manually drawn in MNI space using MicroGL. All ROIs were then registered to each patient's native space through a two-step transformation process. More precisely, the ROIs were first aligned from MNI to the patient's T_1-weighted anatomical image, and then from the T_1 to the diffusion space.

Arcuate fasciculus: Three segments of the AF were reconstructed based on the anatomical definitions from [42]. The seed and target regions were extracted from the AAL atlas, while inclusion ROIs were manually drawn based on anatomical markers described in Dissecting white matter pathways: A neuroanatomical approach by Forkel et al. (2023) [42]. Table 3.1 presents the seed and target ROIs defined for the three segments of the AF, while Figure 3.3 illustrates their anatomical locations. The inclusion ROIs used for the reconstruction of the long and anterior segments are shown in Figure 3.4, and those for the posterior segment are displayed in Figure 3.5. The corresponding tracts are illustrated using an atlas representation in Figure 3.6.

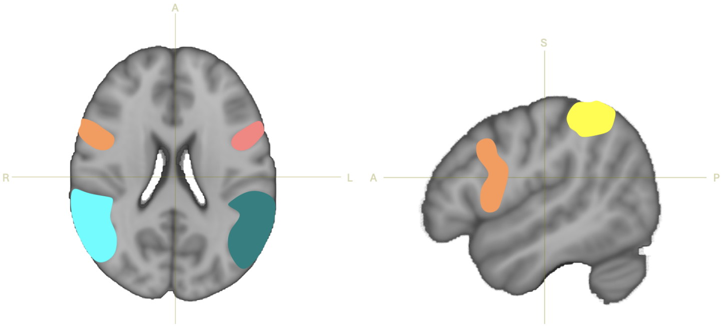

Figure 3.3: Visualization of the regions used as seeds (in orange for the right long and anterior AF, in pink for the left long and anterior AF) and as targets (in light blue for the right long and posterior AF, in green for the left long and posterior AF). The yellow region corresponds to the target of the right anterior AF, also serving as a seed for the right posterior AF.

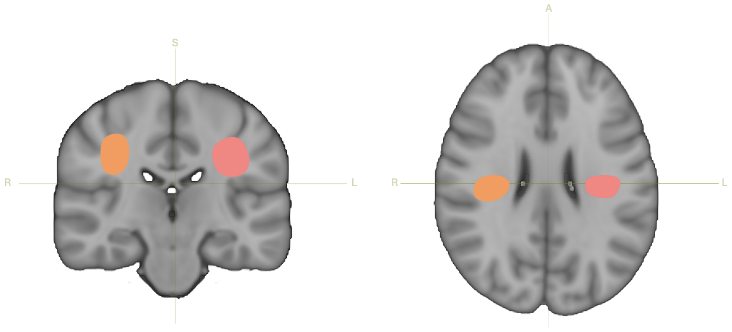

Figure 3.4: Inclusion ROIs for the anterior and long segments of the AF. The inclusion ROIs used to reconstruct the anterior and long segments of the AF are shown in pink for the left hemisphere and in orange for the right hemisphere.

Tract segment	**Seed ROI**	**Target ROI**
Long AF	Opercular part of Inferior Frontal Gyrus	Superior Temporal Gyrus, and Middle Temporal Gyrus
Anterior AF	Opercular part of Frontal Inferior Gyrus	Parietal Inferior Gyrus
Posterior AF	Parietal Inferior Gyrus	Superior Temporal Gyrus, and Middle Temporal Gyrus

Table 3.1: Anatomical ROIs used for AF tracking, based on the AAL atlas and anatomical references in [42].

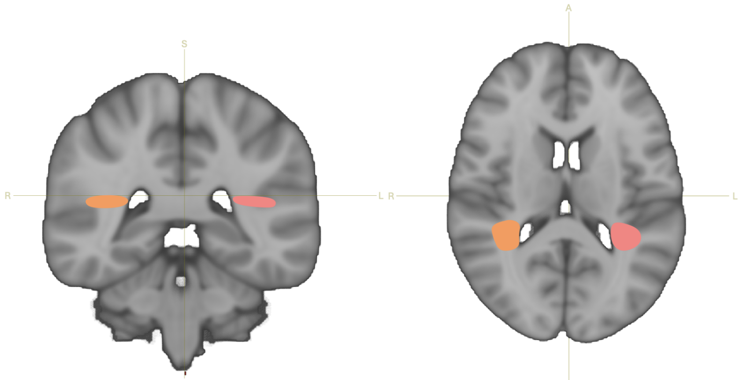

Figure 3.5: Inclusion ROIs for the posterior segment of the AF. The inclusion ROIs used to reconstruct the posterior segment of the AF are shown in pink for the left hemisphere and in orange for the right hemisphere.

Inferior fronto-occipital fasciculus: The seed and target ROIs were defined using the AAL atlas, while the inclusion ROI was manually delineated in the external capsule, following anatomical markers described in Dissecting white matter pathways: A neuroanatomical approach by Forkel et al. (2023) [42]. These ROIs are displayed in Figure 3.7, while the corresponding tracts are illustrated using an atlas representation in Figure 3.11.

- Seed ROIs: Middle and inferior parts of the orbital frontal gyrus, triangular part of the inferior frontal gyrus
- Target ROIs: Superior, middle, and inferior occipital gyri
- Inclusion ROI: External capsule.

Corpus callosum: The CC ROIs were drawn to include all fibers crossing the midsagittal section of the corpus callosum. Due to this topographic and functional organization, the corpus callosum was subdivided into five distinct segments in the present study, in order to better characterize potential microstructural differences. The division of the CC is illustrated in Figure 3.8a and its representation in the brain in Figure 3.8b, while the corresponding tracts are illustrated using an atlas representation in Figure 3.9. The seed and target ROIs included bilateral fronto-parietal, occipital, and temporal cortices [42].

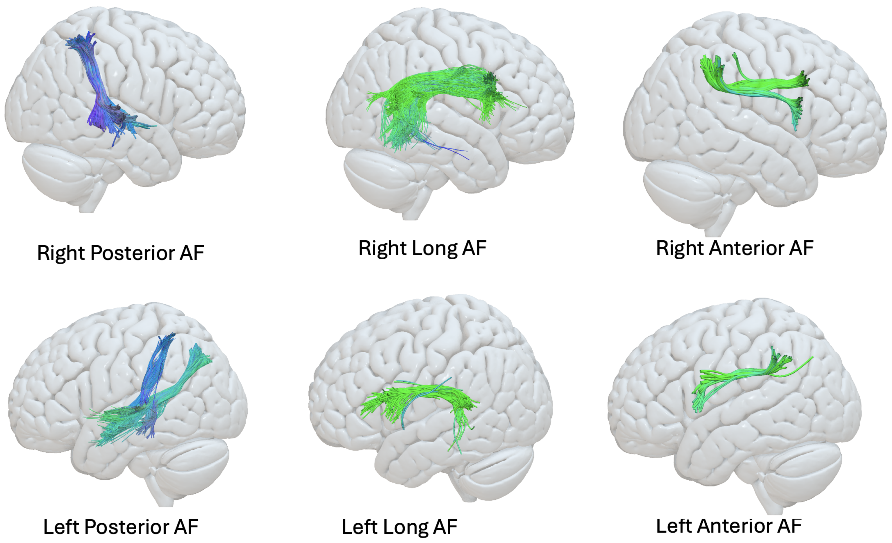

Figure 3.6: 3D visualization of the three AF segments reconstructed in MNI152 standard space.

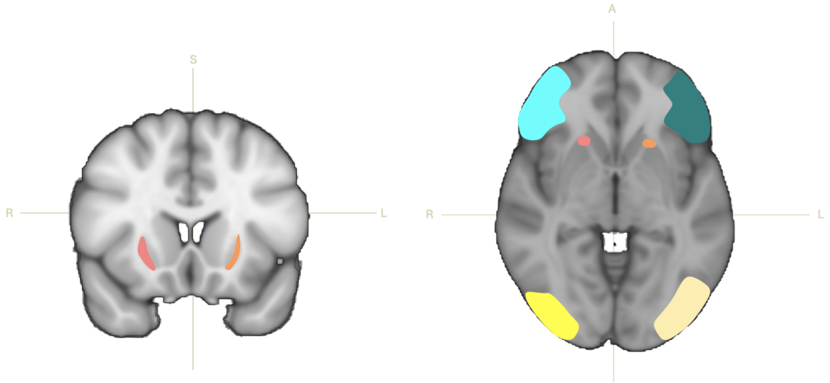

Figure 3.7: Inclusion Region of the right and left IFOF. In pink, the left external capsule. In orange, the right external capsule. In light blue and green, the right and left seed respectively. In dark and light yellow, the right and left target respectively.

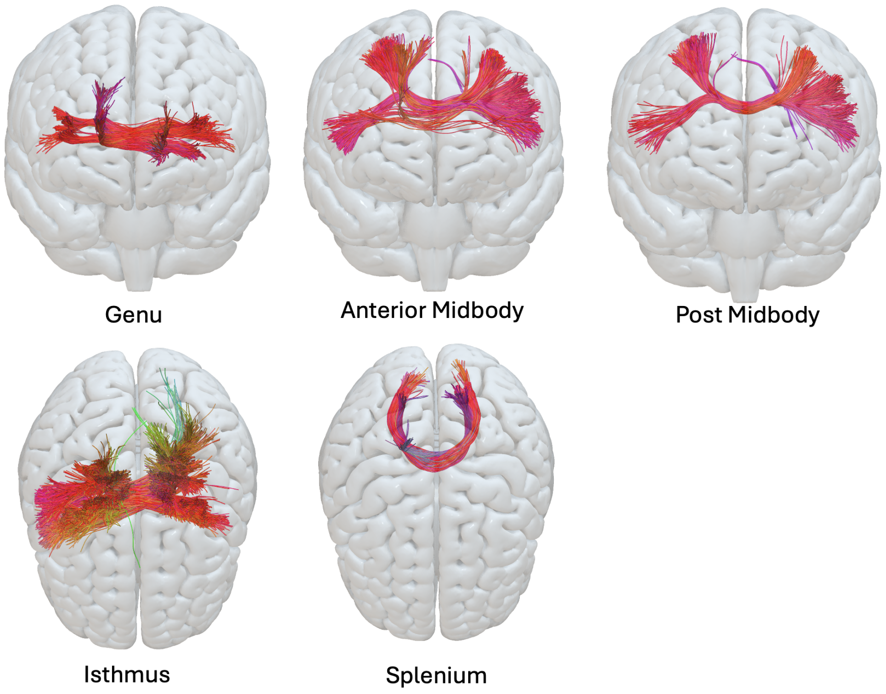

Figure 3.9: 3D visualization of the five CC parts reconstructed in MNI152 standard space.

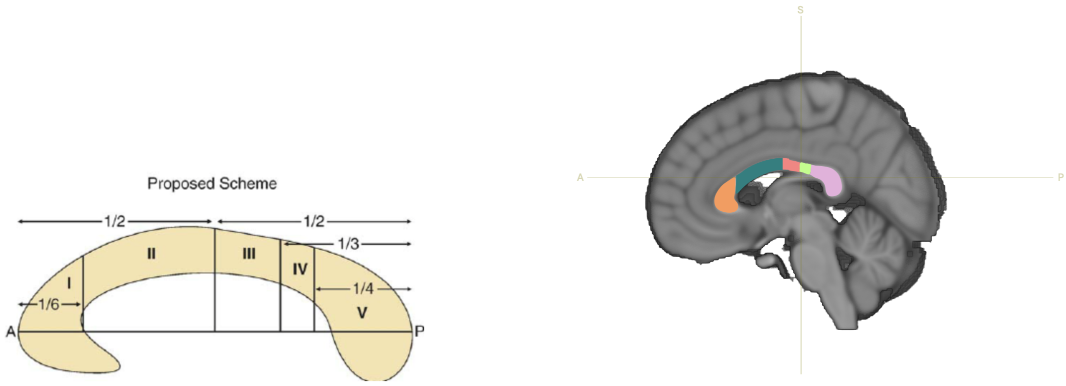

(a) Representation of the division of the CC into five parts. I: Genu; II: Anterior Midbody; III: Posterior Midbody; IV: Isthmus; V: Splenium [76].

(b) Orange : Genu; Blue : Anterior Midbody; Pink : Posterior Midbody; Green : Isthmus; Lila : Splenium

Figure 3.8: Illustration of the five sections of the CC.

Uncinate fasciculus: ROIs were extracted from the AAL atlas. The seed region included the anterior temporal pole, and the target ROI was the orbitofrontal cortex. The tract runs through the ventral portion of the external capsule, which served as an inclusion ROI [42]. The ROIs are shown in Figure 3.10, while the corresponding tract is illustrated using an atlas representation in Figure 3.11.

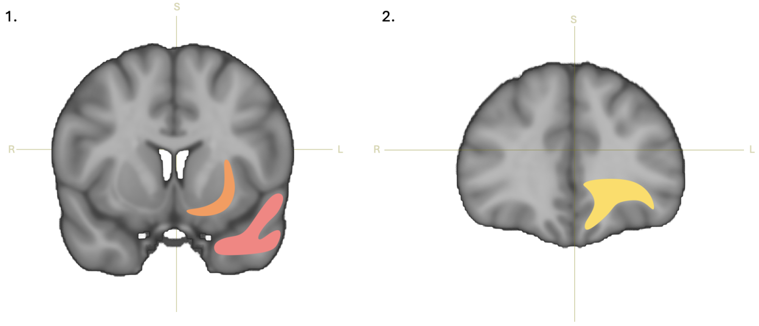

Figure 3.10: ROIs used for the reconstruction of the UF. The orange region indicates the inclusion ROI, and the pink region corresponds to the target ROI. The yellow region represents the seed ROI.

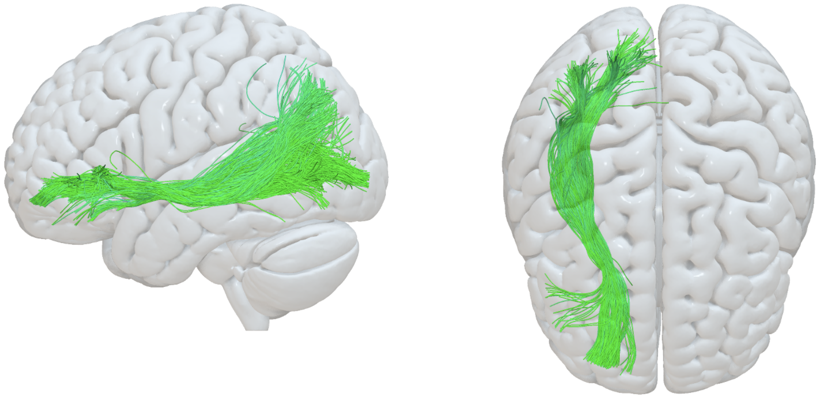

Left IFOF

Right IFOF

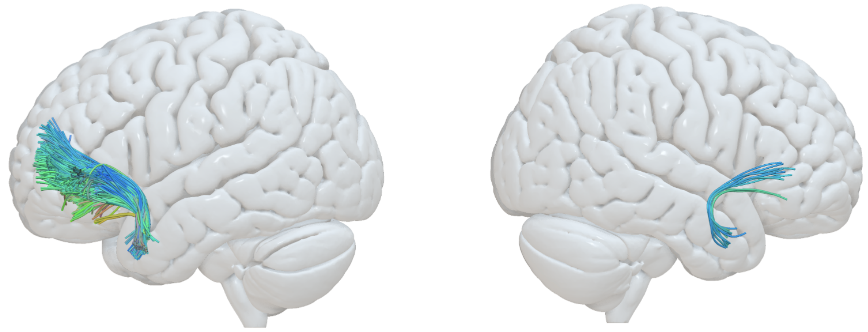

Left UF

Right UF

Figure 3.11: 3D visualization of the left and right UF and the left and right IFOF reconstructed in MNI152 standard space.

3.5.2 Tractography parameters

Tractography was performed on the preprocessed diffusion data using a ROI-based approach. Streamlines were generated using the tckgen command from the MRtrix3 toolbox, employing the probabilistic algorithm iFOD2 (second-order Integration over Fiber Orientation Distributions) [77] for local fiber orientation modeling. Table 3.2 summarizes the main tracking parameters used for each tract. These values were optimized manually for anatomical plausibility and to minimize spurious streamlines.

Tract	Side	Streamlines	Angle (°)	Max Length	Max Attempts	Cutoff
cc genu	—	6000	10	175	4000	0.17
cc ant midbody	—	6000	10	175	4000	0.17
cc post midbody	—	6000	10	175	2000	0.17
cc isthmus	—	7000	10	175	7000	0.13
cc splenium	—	6000	10	175	5000	0.22
uf	left	5000	13	200	6000	0.14
uf	right	5000	13	200	6000	0.19
ifof	left	5000	15	200	6000	0.14
ifof	right	5000	15	200	6000	0.14
af_long	left	4000	10	200	5000	0.13
af_long	right	4000	10	200	4000	0.15
af_post	left	4000	15	150	4000	0.23
af_post	right	6000	15	150	6000	0.23
af_ant	left	4000	10	150	6000	0.2
af_ant	right	5000	10	150	6000	0.22

Table 3.2: Tracking parameters for each tract. Values were manually adjusted for anatomical accuracy and streamline quality.

3.5.3 Tract Filtering

Once the tractographies were generated, a filtering process was applied to eliminate aberrant or isolated streamlines. This step was performed using the Python library `Unravel`, which enables the removal of streamlines that deviate significantly from the average trajectory of the tract [78]. The method computes the distance between each streamline and the mean trajectory: if a streamline deviates excessively for more than half of its length, it is considered an outlier and removed. In this study, the approximate number of neighboring streamlines required for a streamline to be retained was set to 1. Figure 3.12 visually illustrates the result of this filtering step on the left IFOF tract of a representative subject.

3.5.4 Tract Clustering

After generating individual tracts for each patient, both processed and unprocessed tracts were subdivided into eight clusters using the Python library `Unravel` (see Figure 3.13). This method relies on the resampling of a representative streamline, typically the one passing through regions of highest density, into a fixed number of regularly spaced nodes. This subdivision enables the extraction of local diffusion metrics at different segments along each tract.

Once clustering was completed, the direction of cluster numbering was verified for each tract. Indeed, some tracts may have been oriented in the opposite direction compared to others, which would make inter-subject comparisons inconsistent. Figure 3.14 illustrates this verification step: blue points represent the centroids of

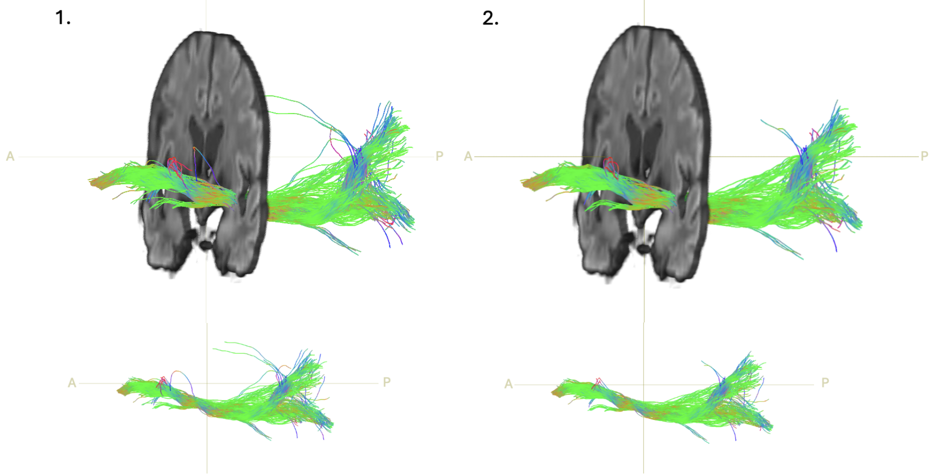

Figure 3.12: Example of filtering applied to the left IFOF: 1) before filtering; 2) after filtering with neighborhood threshold = 1

the first cluster (start point), while red points indicate the centroids of the last cluster (end point). Grey lines connect the extremities of the average streamline for each subject. When inconsistencies in orientation were detected, as in the case of the left uncinate fasciculus, a manual inversion of cluster numbering was performed to align them with the majority direction. To identify such inconsistencies, the spatial coordinates of the centroids of the first (Cluster 1) and last (Cluster 8) segments were compared across subjects. Specifically, the anatomical axis relevant to each tract (e.g., z-axis for the UF) was used to determine whether the start and end points followed a consistent direction across patients. When a subject's tract deviated from the dominant pattern, the cluster labels were reversed (i.e., Cluster 1 became 8, 2 became 7, etc.) to standardize the orientation across all subjects. In contrast, tracts such as the left IFOF already exhibited consistent cluster orientations across all subjects. Verification plots for the remaining tracts are available in Appendix C.

3.5.5 Metrics extraction and computation

Once the orientation of cluster numbering was corrected across subjects, diffusion metrics (FA, MD, AD, RD) were extracted from each subject's tractography data using the libraries `Nibabel 5.2.1`, `NumPy`, `Pandas`, and the tractography analysis package `Unravel`. For each tract, values were computed both at the whole-tract level and separately for each of the eight clusters. In both cases, measurements were averaged with a binary mask indicating the presence of current lines in each voxel.

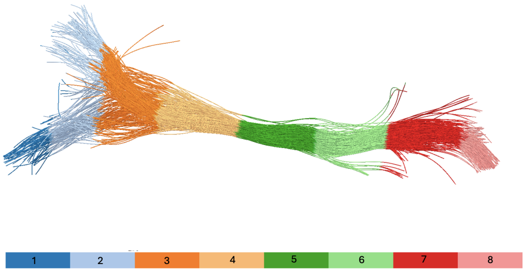

Figure 3.13: Visualization of the left IFOF clustered into eight segments. Each color represents a cluster of the tract, ranging from segment 1 (dark blue) to segment 8 (light red). This segmentation was obtained using the algorithm provided by the `Unravel` library.

The diffusion values obtained were used in statistical analyses of their association with measures of auditory performance.

3.6 Statistical Analysis

A series of non-parametric statistical analyses was conducted to evaluate the relationship between microstructural diffusion measures and behavioural performance for both processed and unprocessed tracts.

First, Spearman correlations were computed between patient characteristics (age and duration of hearing aid use) and behavioural scores from the DEWA and AWRS tests at various pre- and post-operative time points. The aim of this preliminary analysis was to identify potential confounding variables to be controlled for in subsequent analyses.

The main analyses initially focused on mean diffusion metrics computed across entire white matter tracts. For each tract, Spearman correlations were performed between the global values of FA, MD, AD, and RD, and the behavioural scores from the DEWA and AWRS tests at pre-implantation and at 6 months post-implantation. In total, 240 tests were conducted (15 tracts × 4 diffusion metrics × 4 behavioural scores). Based on the behavioural scores that showed significant associations in these correlations (see section Behavioral Data Analysis), partial correlations were subsequently conducted to evaluate the relationship between tract-level diffusion metrics and DEWA and AWRS scores at 12 months post-implantation, controlling for age, using the `pingouin 0.5.5` package. This resulted in an additional 120 tests.

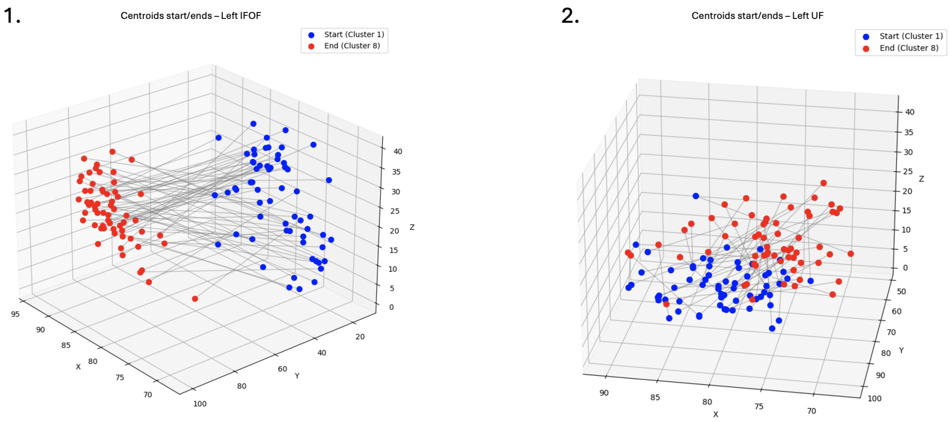

Figure 3.14: Orientation verification for the left IFOF and left UF. Each point represents the centroid of the first (blue) or last (red) cluster for one subject. Grey lines connect the extremities of the average streamline. For the IFOF (1), all subjects show a consistent numbering direction. In contrast, the UF (2) displays inconsistencies across subjects, requiring manual reordering of clusters to ensure comparability.

A separate Spearman correlation analysis was also performed between the four diffusion metrics and the change in DEWA scores over time (i.e., 6 months minus pre-implantation, and 12 months minus pre-implantation), leading to another 120 tests.

To investigate microstructural-functional relationships at a finer spatial scale, cluster-wise analyses were performed on the tracts identified as relevant in the whole-tract analyses. Each tract was subdivided into eight segments, and Spearman correlations were computed between the mean FA, MD, AD, and RD values of each cluster and the behavioural outcomes.

To control the risk of false positives (type I errors) due to the large number of statistical tests performed, a multiple comparison correction was applied using the False Discovery Rate (FDR) method, specifically the Benjamini–Hochberg procedure [79]. This method controls the expected proportion of false discoveries among the rejected hypotheses.

The Benjamini–Hochberg procedure consists in sorting all p-values from smallest to largest ($p_{(1)} \leq p_{(2)} \leq \cdots \leq p_{(m)}$), where m is the total number of tests performed. For a given false discovery rate level q, each p-value p_i is compared to its critical value defined as:

$$p_i \leq \frac{i}{m} q$$

The largest p_i satisfying this inequality is considered statistically significant, and all p-values ranked before it are also declared significant, even if they are not individually below their own critical threshold.

In line with McDonald's guidance on balancing discovery and statistical stringency [80]:

> *"If the cost of additional experiments is low and the cost of a false negative (missing a potentially important discovery) is high, you should probably use a fairly high false discovery rate, like 0.10 or 0.20, so that you don't miss anything important."*

and given the exploratory nature of this study, two FDR thresholds were considered for multiple comparison correction:

- Results with $q < 0.05$ were considered statistically significant.
- Results with $0.05 \leq q < 0.10$ were interpreted as *trends* worth further investigation.

All statistical analyses were performed using Python, primarily with the `pandas 2.2.3` and `scipy.stats 1.15.1` libraries for correlation testing, and FDR correction for multiple comparisons.

Chapter 4

Results

This section presents the results of our investigation into the relationship between white matter microstructure and speech perception outcomes in cochlear implant patients. It begins with the correlations between behavioural measures, followed by the visualisation of the tracts generated from the regions of interest described in Section 3.5.1. Finally, we report the correlations between behavioural outcomes and diffusion metrics extracted from the tracts.
Unless otherwise specified, streamline color coding follows the standard convention based on local main orientation: red indicates left–right, green indicates anterior–posterior, and blue indicates superior–inferior. Abbreviations used in the figures include: R = right, L = left, A = anterior, P = posterior, S = superior. A summary of the audiometric variable names and their corresponding meanings is provided in Appendix A.

4.1 Behavioral Data Analysis

Before performing correlation analyses, we assessed the distribution of the variables of interest, including the age and the audiometric test scores. The histograms presented in figure 4.1 allow us to visually inspect their shape in order to conclude that the behavioral data do not follow a normal distribution. This justifies the use of Spearman's rank correlation, a non-parametric method, to examine the relationship between age or hearing aid usage duration and audiometric outcomes (AWRS and DEWA, both pre- and post-implantation).

Table 4.1 summarizes the results of these analyses. Age shows significant negative correlations with auditory performance at 12 months post-implantation, particularly for the AWRS test (*AWRS_12m*, $p < 0.001$) and the DEWA test (*dewa_12m*, $p = 0.011$). In contrast, no significant correlation was found between the duration of hearing aid use and pre- and post-implant performance. Given the association

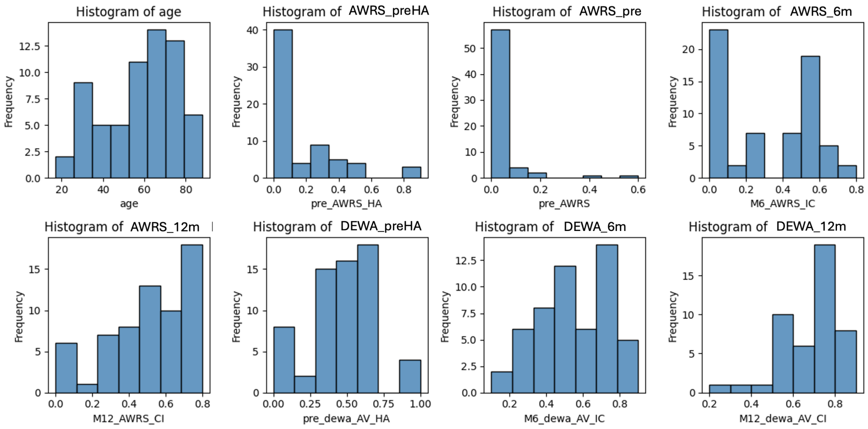

Figure 4.1: Distribution of the age and audiometric test scores across the sample. These histograms help assess the normality and variability of each variable prior to correlation analysis.

with age, this variable was controlled for in the subsequent correlation analyses through partial correlation procedures.

Variables	Audiometric Tests	Spearman Coefficient	p-value
age	ARWS_preHA	−0.048	0.707
age	AWRS_pre	−0.099	0.434
age	AWRS_6m	−0.187	0.136
age	AWRS_12m	**-0.514**	**<0.0001**
age	dewa_preHA	−0.190	0.135
age	dewa_6m	−0.220	0.114
age	dewa_12m	**-0.370**	**0.011**
age	diff_dewa_6m	−0.042	0.766
age	diff_dewa_12m	−0.205	0.177
duration_HA	ARWS_preHA	−0.156	0.220
duration_HA	ARWS_pre	−0.221	0.080
duration_HA	AWRS_6m	−0.208	0.099
duration_HA	AWRS_12m	−0.168	0.191
duration_HA	dewa_preHA	−0.088	0.499
duration_HA	dewa_6m	0.005	0.973
duration_HA	dewa_12m	−0.251	0.093
duration_HA	diff_dewa_6m	0.205	0.144
duration_HA	diff_dewa_12m	−0.005	0.973

Table 4.1: Spearman correlations between age or duration of hearing aid use (duration_HA) and various audiometric scores. Significant results are shown in bold.

To better understand interindividual differences in post-operative improvement, the relationship between pre-operative performance and the evolution of audiometric scores was examined. Figure 4.2 presents the correlation between pre-implant scores and post-operative improvement for the DEWA and AWRS tests, at 6 and 12 months post-implantation.

4.2 Tractography Results

All tracts of interest were successfully reconstructed in all participants. However, some interindividual variability in streamline density was observedand is illustrated in Figure 4.3. These differences may reflect anatomical variability or differences in data quality.

Visual inspections were performed to ensure anatomical consistency and segmentation quality, supporting the validity of the tractography methodology. The three segments of the AF are shown in Figure 4.4, the left and right IFOF in Figure 4.5, and the UF in Figure 4.6. Finally, the five subdivisions of the CC are displayed in Figure 4.7.

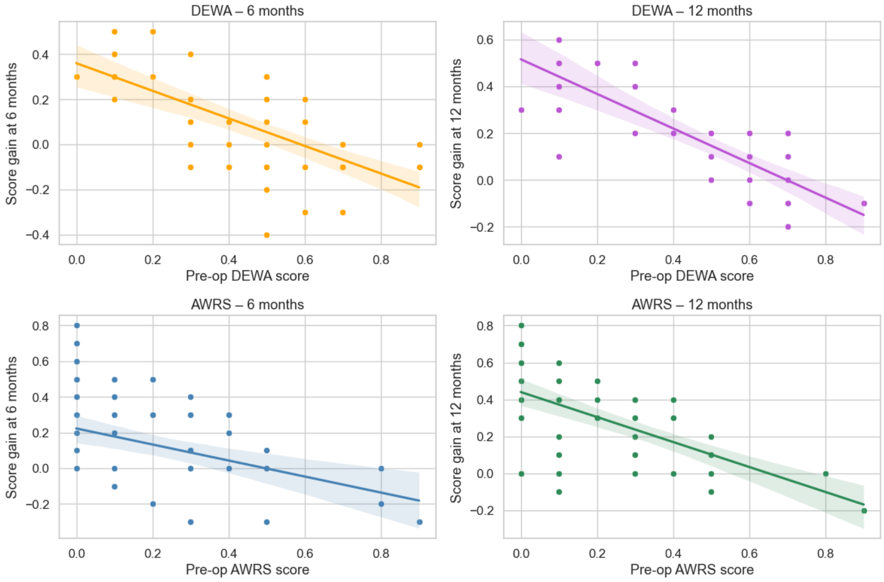

Figure 4.2: Ceiling effect in DEWA and AWRS scores at 6 and 12 months. Each scatterplot shows the relationship between pre-operative test scores (x-axis) and subsequent improvement (y-axis), calculated as the difference between post- and pre-implantation performance.

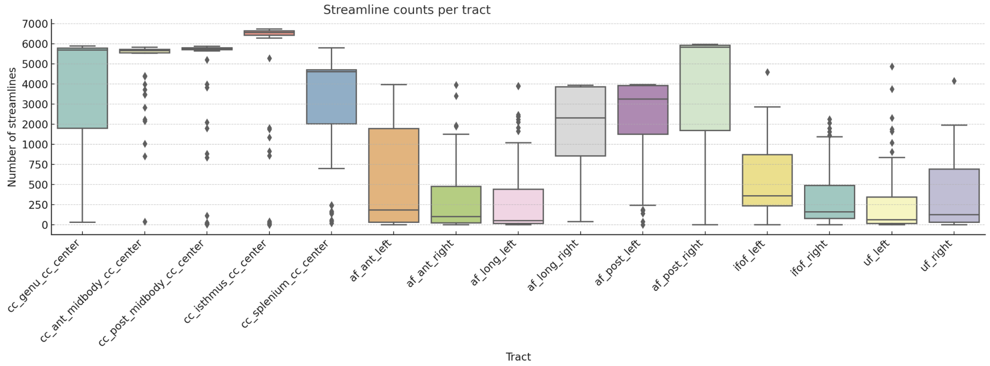

Figure 4.3: Streamline counts per tract. Boxplot showing the distribution of the number of streamlines reconstructed for each white matter tract across participants. The y-axis is scaled non-linearly to preserve visibility of both low and high streamline counts.

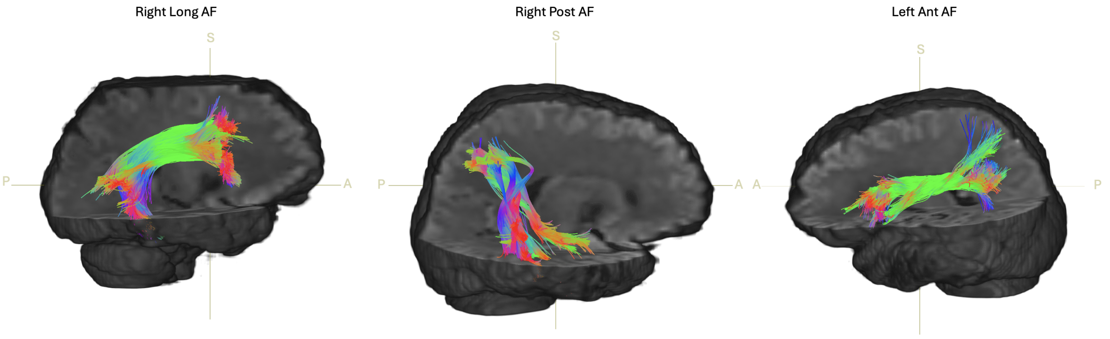

Figure 4.4: Visualization of the right long, right posterior, and left anterior segments of the AF of representative subjects.

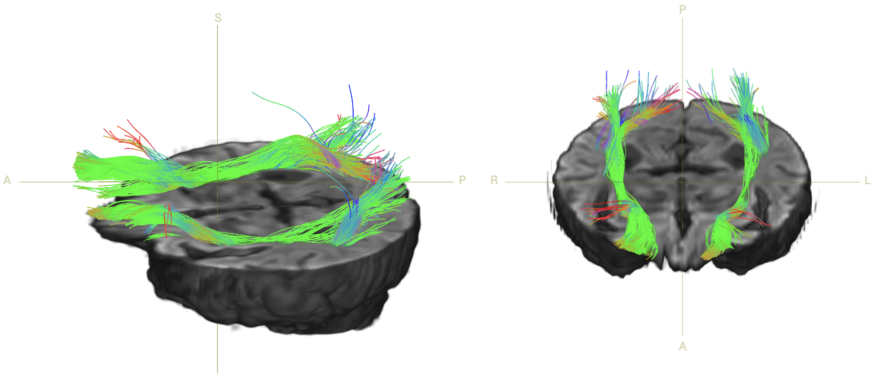

Figure 4.5: Left and right IFOF segments visualization for a representative subject.

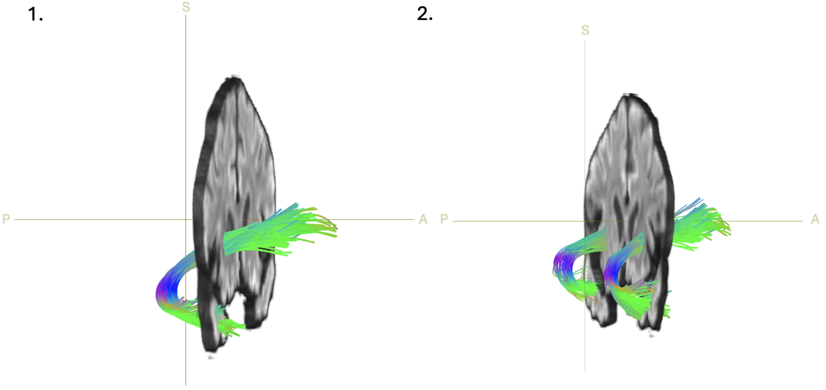

Figure 4.6: UF representation on a subject. 1. Right UF 2. Left and right UF.

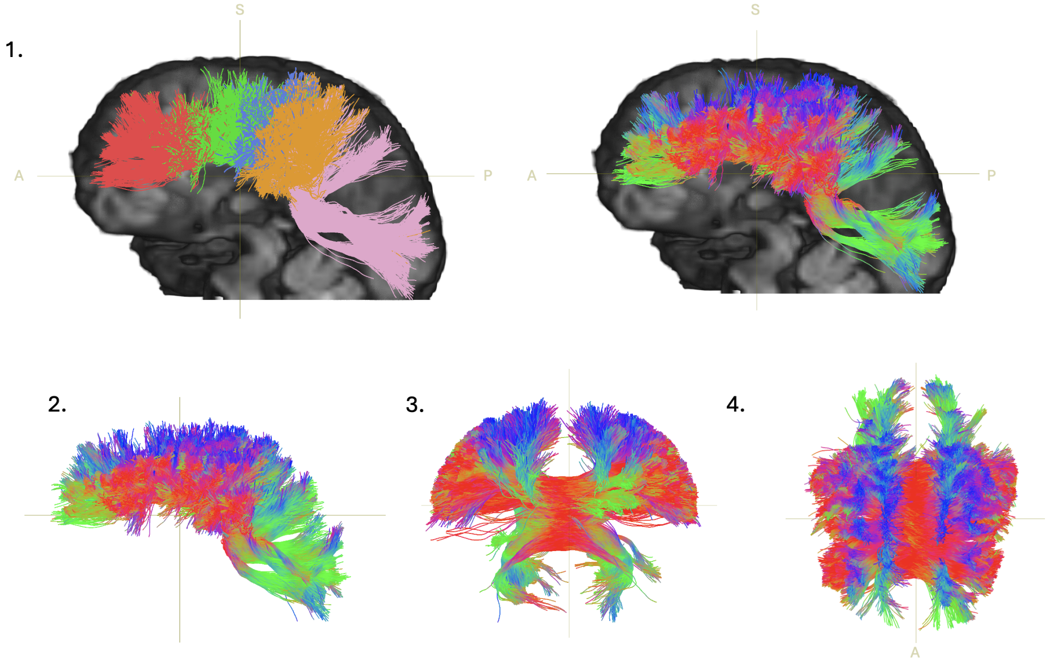

Figure 4.7: 1. Illustration showing the five corpus callosum subdivisions used in the study: genu (red), anterior midbody (green), posterior midbody (blue), isthmus (orange), and splenium (pink). 2. Sagittal view of all reconstructed tracts for a representative subject. 3. Coronal view, 4. Axial (top-down) view of the same tractogram.

4.2.1 FA Distribution across Clusters

Following the extraction of diffusion metrics per cluster, Figure 4.8 presents the distribution of FA values across the eight segments for each tract. Most tracts show higher FA in central clusters and lower values at the extremities.

4.3 Statistical Analysis of Tract-Audiometry Relationships

This section reports the statistical correlations between white matter microstructure, measured via DTI metrics, and auditory scores at pre-implantation, as well as at six and twelve months post-implantation. It also includes correlation analyses between diffusion metrics and the evolution of audiometric performance from pre-implantation to six and twelve months post-implantation.

4.3.1 Whole-tract analysis

The Spearman correlation analysis between non-processed whole-tract mean diffusion metrics and audiometric scores at pre-implantation and six months post-implantation revealed several statistically significant associations after correction for multiple comparisons using the FDR method (threshold $q = 0.05$).

Left Posterior AF. The left posterior AF showed significant negative correlations with the DEWA scores at both pre-implantation and six months post-implantation:

- MD and *DEWA_6m* (ρ = -0.502; *p-FDR* = 0.027),
- RD and *DEWA_6m* (ρ = -0.481; *p-FDR* = 0.027),
- RD and *DEWA_preHA* (ρ = -0.432; *p-FDR* = 0.027).

Right IFOF. A significant negative correlation was also observed between AD in the right IFOF and DEWA scores at six months post-implantation (ρ = -0.478; *p-FDR* = 0.027).

No significant correlations were found between diffusion metrics and the AWRS scores at six months post-implantation. Also, no statistically significant correlations were found between any diffusion metric and the audiometric outcomes at twelve months post-implantation, even when applying a more permissive FDR threshold

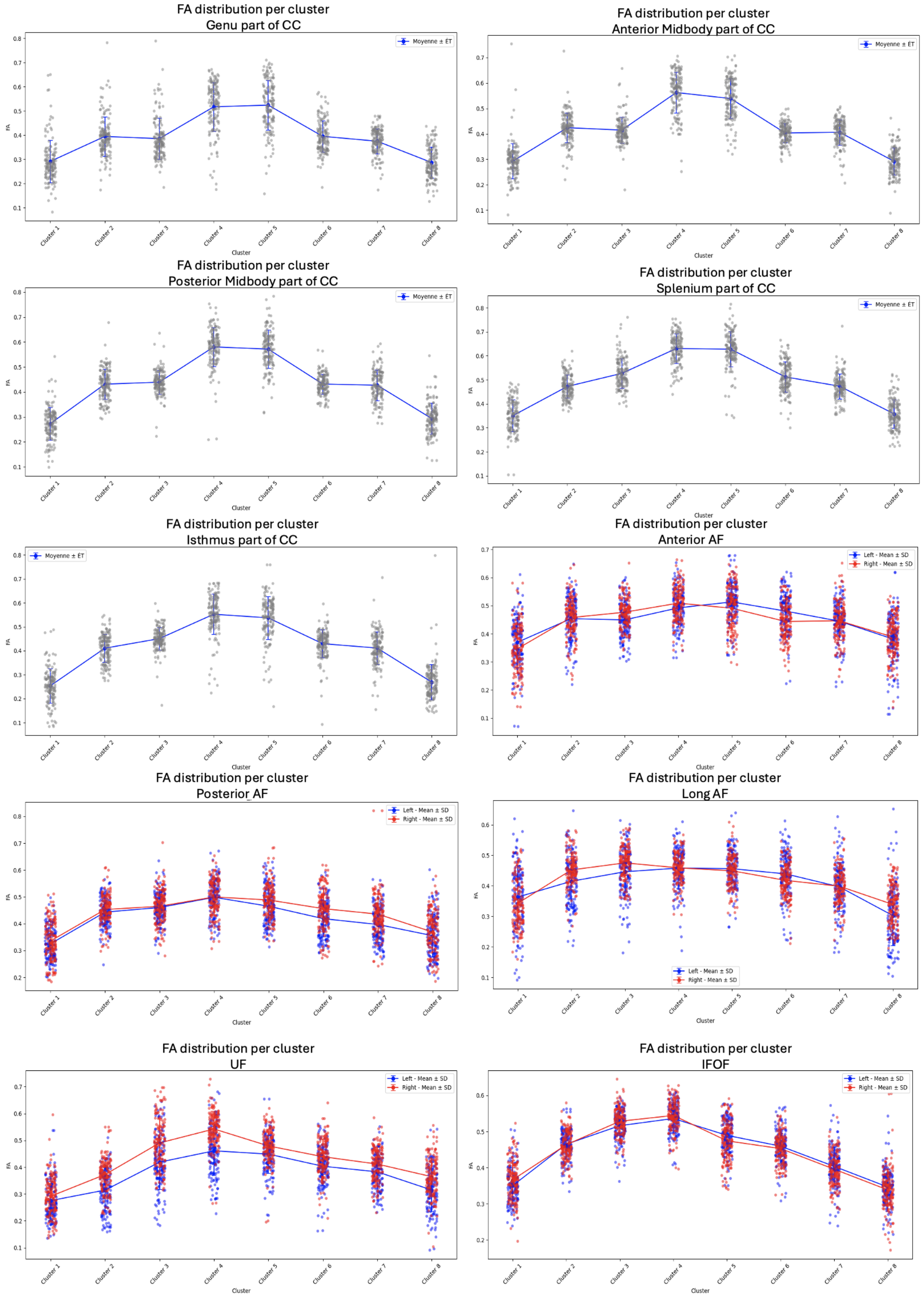

Figure 4.8: Each plot shows the individual FA values (dots) for each of the 8 clusters along the tract trajectory. Mean FA values ± standard deviation (SD) are overlaid as lines for both hemispheres: blue for the left hemisphere, and red for the right hemisphere.

($q = 0.1$).

Additionally, correlations between the diffusion metrics and the evolution scores (difference between post- and pre-implantation scores) at six and twelve months did not produce any statistically significant results, even under a more permissive threshold ($q = 0.1$).

Finally, no significant correlations were identified between diffusion metrics and audiometric scores when considering the filtered tracts.

4.3.2 Cluster-wise analysis

A Spearman correlation analysis was performed between the mean diffusion metrics values of individual tract clusters and audiometric scores based on the results obtained on the whole-tract statistical analysis. After correction for multiple comparisons using the FDR method (threshold $q = 0.05$), several significant correlations were identified between local diffusion metrics and audiometric scores in specific segments of the posterior AF and the right IFOF, as revealed by cluster-wise analysis.

Left Posterior AF. In the left posterior AF, multiple clusters showed significant negative correlations with DEWA scores at both pre- and six-month evaluations. More specifically:

- Cluster 4 showed a strong negative correlation between MD and *dewa_6m* scores (ρ = -0.494, *p-FDR* = 0.022),
- Cluster 5 also showed a significant correlation between MD and *dewa_6m* scores (ρ = -0.490, *p-FDR* = 0.022),
- A significant correlation was also found between AD and *dewa_6m* in Cluster 4 (ρ = -0.475, *p-FDR* = 0.024),
- Additionally, a negative correlation was observed between RD and *dewa_6m* in Cluster 5 (ρ = -0.430, *p-FDR* = 0.035),
- Finally, pre-operative DEWA scores were negatively correlated with MD (ρ = -0.400, *p-FDR* = 0.035) and RD (ρ = -0.386, *p-FDR* = 0.039) in Cluster 4 , and with RD in Cluster 2 (ρ = -0.400, *p-FDR* = 0.035).

Figure 4.9 illustrates the anatomical location of the three clusters within the left posterior AF that were significantly associated with pre- and post-implantation DEWA performance. Cluster 2 is likely located in the left inferior parietal lobule,

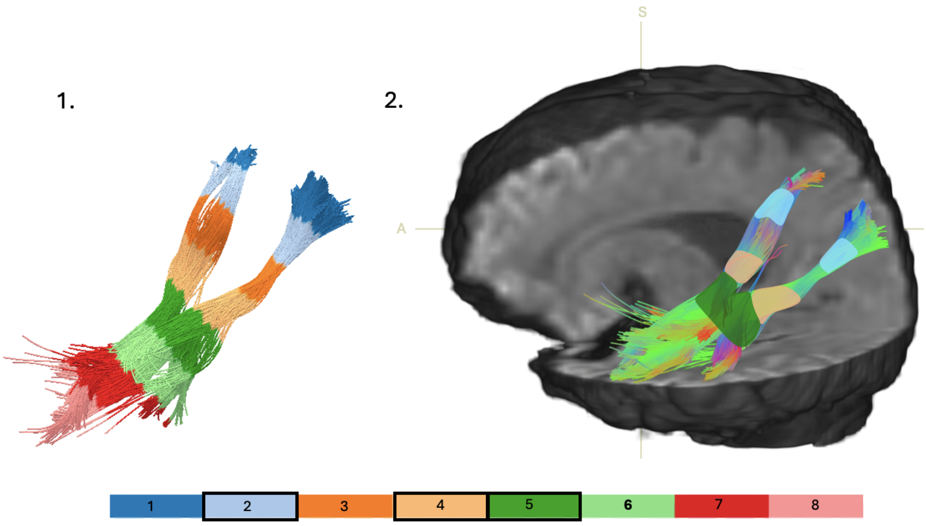

Figure 4.9: Visualization of the left posterior AF and its cluster-wise segmentation. 1. Whole-tract segmentation into eight clusters. 2. Visualization of the three clusters that showed significant correlations with DEWA scores in a representative subject.

Cluster 4 may overlap with the left optic radiations, and Cluster 5 appears to be situated in the left STG.

Right IFOF. In the right IFOF, a significant negative correlation was found between RD in Cluster 6 and *dewa_6m* scores (ρ = -0.431, *p-FDR* = 0.035), indicating that local microstructural properties in this segment may also contribute to audiovisual speech processing outcomes. Figure 4.10 illustrates the anatomical location of the cluster within the right IFOF.
Cluster 6 is located in the region of the external capsule, a white matter structure situated between the putamen and the claustrum, through which the IFOF courses on its path to the frontal lobe.

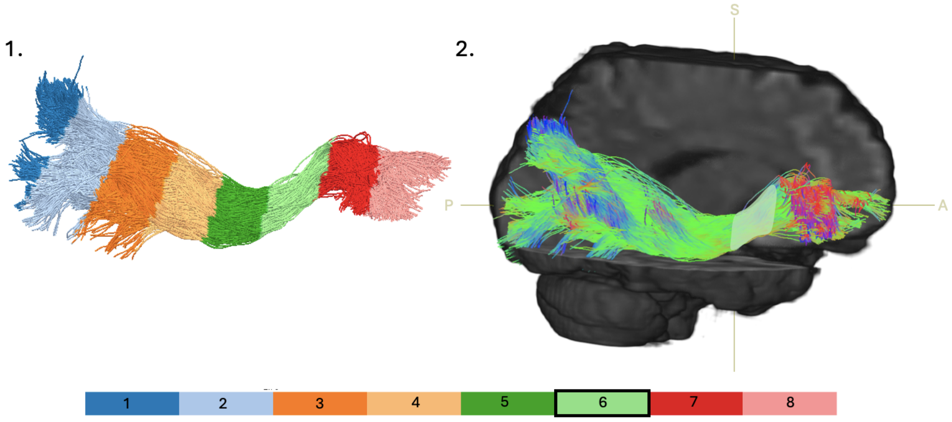

Figure 4.10: Visualization of the right IFOF and its cluster-wise segmentation. 1. Whole-tract segmentation into eight clusters. 2. Visualization of the cluster that showed significant correlations with DEWA scores in a representative subject.

Chapter 5

Discussion

This chapter evaluates the extent to which white matter microstructure, as assessed through tractography, can serve as a biomarker of auditory rehabilitation success after cochlear implantation. It also discusses the strengths and limitations of the tractography-based methodology used in this study, including factors related to diffusion imaging quality, behavioural test sensitivity, and perspectives for improving.

5.1 Results Interpretation

5.1.1 Whole-tract Analysis

Significant associations at pre-operative and six-month evaluations

Whole-tract analyses revealed significant correlations between diffusion metrics and DEWA scores at six months post-implantation for the left posterior AF and the right IFOF. Additionally, a significant correlation was found between RD and DEWA scores in the left posterior AF at the pre-implantation stage. No significant associations were observed with twelve-month outcomes or with AWRS scores at any time point.

Left posterior AF: a key tract for speech comprehension

The results indicate that microstructural integrity in the left posterior AF is significantly associated with speech comprehension performance at pre-implantation and six months post-implantation, as measured by the *dewa_preHA* and the *dewa_6m* score. The DEWA test assesses the comprehension of monosyllabic words presented in auditory, visual, and audiovisual conditions, and is designed to evaluate audiovisual integration and speech perception capabilities.

The posterior segment of the AF is anatomically implicated in semantic processing and lexical memory [15, 37], and its involvement in speech comprehension is supported by prior studies. Notably, Ivanova et al. [60] demonstrated that damage to this segment was associated with deficits in auditory comprehension, naming, and repetition in patients with post-stroke aphasia.

In this context, the observed negative correlations between *dewa_6m* and both MD and RD in addition to the negative correlation between *dewa_preHA* and RD in the left posterior AF are consistent with the interpretation that lower diffusivity values reflect better white matter organization [35], which may support more efficient auditory and audiovisual processing.

Right IFOF: balancing verbal and non-verbal semantic pathways

In addition to the posterior AF, the results revealed significant moderate negative correlation (ρ = -0.478) between the *dewa_6m* score and AD in the right IFOF. These findings suggest that lower AD in this tract may also support improved speech comprehension in audiovisual contexts.

The IFOF has been implicated in visual object recognition, semantic processing, and lexical retrieval [38]. Furthermore, direct electrical stimulation of the IFOF has been shown to induce anomia without visual impairments, reinforcing its role in lexical-semantic access [18]. More precisely, the right IFOF has been implicated in non-verbal semantic processing and mentalizing [39, 63, 81].

Interestingly, reduced AD in the right IFOF was associated with better performance on the audiovisual DEWA test at six months post-implantation. While decreased AD is classically interpreted as a marker of axonal injury [34], studies have noted that in regions of high fiber complexity, such as those with crossing fibers, the reliability of tensor-based AD estimates is limited [13]. One possible interpretation is that reduced AD in this region reflects a downregulation of compensatory reliance on visual semantic strategies, which may otherwise compete with or hinder the reintegration of auditory processing after implantation. From this perspective, lower AD in the right IFOF might paradoxically support improved auditory outcomes by rebalancing the contribution of non-verbal semantic systems. Nonetheless, this result should be interpreted with caution, and further research is needed to clarify the underlying mechanisms.

No associations at twelve months: evidence for a plateau effect

No significant correlations were observed between diffusion metrics and audiometric scores at twelve months post-implantation. This lack of association could be explained by the temporal trajectory of cochlear implant outcomes. Dillon et al. [82] reported that speech perception performance typically stabilizes between six months and one year post-implantation, with substantial improvements occurring mainly between one and five years.
In our study, the absence of significant associations at twelve months may therefore reflect this plateau phase in auditory recovery.

No correlation with scores evolution: possible ceiling effects

Correlations between diffusion metrics and the evolution of audiometric scores (i.e., the difference between post- and pre-implantation performance) at six months and twelve months post-implantation were also examined. No significant associations were found, even under a more permissive FDR threshold ($q = 0.1$).

One possible explanation is that some participants already had high pre-implantation DEWA scores, leaving little room for measurable improvement, an effect known as a ceiling effect. This could have masked true associations between structural integrity and auditory outcomes. As shown in Figure 4.2, participants with higher pre-operative scores tended to exhibit smaller post-operative gains on both the DEWA and AWRS tests, supporting the presence of this ceiling effect.

Limitations of FA averaging and tract filtering strategies

It is important to note that FA did not show any significant correlations with audiometric outcomes at the whole-tract level, despite being one of the most commonly used DTI metrics. This result may be due to the non-uniform distribution of FA values along the tracts, as visualized in our cluster-based plots (see Figure 4.8). FA tends to peak in the central segments of many tracts and decrease toward their cortical extremities, resulting in a non-linear profile. This pattern likely reflects underlying anatomical differences: streamlines typically traverse highly organized deep white matter (associated with higher FA), before branching into more complex and less coherent fiber structures near the cortical surface, where FA tends to be lower. Consequently, averaging FA across the entire tract may obscure localized microstructural variations that are functionally relevant. This observation reinforces the need for local analyses, such as the cluster-based approach presented in the next section.

Additionally, we compared results obtained using unfiltered tracts to those filtered with a minimum neighborhood criterion (minimum neighbor = 1). Despite expectations, no significant associations were observed in the filtered dataset. This could be due to the averaging strategy: values were computed using a binary mask rather than being weighted by streamline density. As a result, voxels with high streamline density may have contributed equally to those with minimal contributions, potentially diluting the signal. Future studies should investigate the utility of density-weighted averaging approaches, which may provide more anatomically and functionally precise metrics when analyzing whole-tract data.

5.1.2 Cluster-wise Analysis

Cluster analyses were carried out to refine and localize the results of the whole-tract approach. This finer segmentation aimed to identify whether specific subregions within the significant tracts were responsible for the associations observed with speech comprehension scores. The analysis revealed several clusters with significant correlations between diffusion measures and DEWA scores, both pre-implant and six months post-implant. These included three clusters in the left posterior AF and one in the right IFOF.

Left Posterior AF

Cluster 2 - Left Inferior Parietal Lobe Cluster 2, located in the left inferior parietal lobe, showed a moderate and significant negative correlation between RD and pre-operative DEWA scores. This finding suggests that better microstructural integrity in this region is associated with improved audiovisual comprehension abilities prior to implantation.

The inferior parietal lobe plays a central role in the fronto-parietal network of the dorsal language pathway, particularly in phonological processing. It receives input from major white matter tracts such as the superior longitudinal fasciculus III and the posterior segment of the AF, which are involved in integrating auditory perception with verbal articulation [81]. This may explain why microstructural properties in this region correlate with pre-implantation DEWA performance.

Cluster 4 - Likely Left Optic Radiations Cluster 4, likely located in the left optic radiations, exhibited several significant correlations. On the one hand, negative correlations were found between pre-operative DEWA scores and both MD and RD. On the other hand, at six months post-implantation, significant negative correlations were also observed between DEWA scores and both MD and

AD in this region.

These results indicate that better preserved white matter microstructure, reflected by lower MD and RD values, is associated with improved audiovisual performance both before and after implantation [35]. MD is often interpreted as a marker of extracellular space or reduced diffusion barriers: lower MD values are thus generally associated with higher tissue density or more organized microstructure. Similarly, lower RD is typically linked to greater myelination.

However, the interpretation of AD is more complex. Reduced AD is classically associated with axonal injury [34], which appears counterintuitive in the context of improved outcomes. This finding may reflect local structural reorganization or limitations of tensor-based metrics in regions with high fiber complexity or crossing fibers [13].

It is important to note that the inclusion ROI used to generate the tracts may have been drawn in this area, potentially leading to a higher concentration of streamlines and, consequently, an overrepresentation of this region in the statistical analyses. This possibility should be considered when interpreting the results.

Cluster 5 - Left Superior Temporal Region. Cluster 5, located in the posterior portion of the left superior temporal gyrus, showed two significant moderate negative correlations with DEWA scores at six months post-implantation. The first involved MD ($\rho = -0.490$), and the second RD ($\rho = -0.430$). These findings suggest that lower MD and RD values in this region are associated with better audiovisual comprehension outcomes following cochlear implantation.

Reductions in MD and RD are commonly interpreted as indicators of improved white matter integrity [35], which may underlie the better audiovisual comprehension outcomes observed in this region. The involvement of the superior temporal region is also consistent with previous literature: Ivanova et al. [18] reported that the temporal portion of the left AF plays a role in both language comprehension and production.

Moreover, recent evidence from a review by Quatre (2024) [68] indicates that increased RD is frequently observed in the superior temporal cortex of deaf individuals, suggesting that this region is particularly sensitive to sensory deprivation and may undergo structural reorganization in the absence of auditory input. The observed association in our study may thus reflect individual differences in the preservation or recovery of microstructural integrity in this key auditory and language-processing area.

Right IFOF

Cluster 6 - External capsule A moderate and significant negative correlation (ρ = -0.431) was observed between RD in Cluster 6 of the right IFOF, located at the level of the external capsule, and DEWA test scores at six months post-implantation. This finding suggests that lower RD values are associated with better audiovisual comprehension performance, and thus with more favorable post-operative outcomes.

RD is considered a marker of white matter microstructure, particularly of myelin integrity. Increased RD has been linked to demyelination or axonal degeneration [13, 35]. Therefore, lower RD may reflect improved structural organization in this region.

Recent findings reinforce the clinical relevance of this area in auditory processing. Huang et al. [65] reported that, in patients with sensorineural hearing loss, the degree of auditory deprivation was associated with decreased FA and increased MD, AD, and RD values in the right external capsule. These microstructural alterations were significantly correlated with the severity of hearing loss. This findings supports the notion that the external capsule, and by extension the right IFOF, may undergo reorganization in response to auditory deprivation, influencing its role in post-implantation outcomes.

Additional support for the functional specialization of this region comes from Roux et al. [63], who demonstrated that the right IFOF can be functionally stratified into two subcomponents: a dorsal portion, involved in mentalizing (i.e., the ability to infer others' mental states from subtle visual cues, such as eye expressions), and a ventral portion, supporting non-verbal semantic processing. The external capsule, where the cluster is located, has been identified as a key passage point for the dorsal fibers of the IFOF associated with mentalizing.
Furthermore, Sarubbo et al. [81] showed, using the Palm-Pyramid-Tree test of non-verbal semantic comprehension, that stimulation of the ventral third of the external capsule, along the trajectory of the right IFOF, could induce deficits in non-verbal semantic processing.

In our study, the DEWA test assesses the comprehension of monosyllabic words under auditory, visual, and audiovisual conditions. Therefore, it relies on multisensory integration, potentially engaging both verbal and non-verbal semantic systems. The anatomical location of the cluster within this functionally diverse region may thus explain the observed association between local microstructure and DEWA performance six months after cochlear implantation.

5.2 Limitations

5.2.1 Sample Characteristics

One important limitation of this work is the sample size, which may limit the generalizability of the results and reduce statistical power. Although age was controlled for in partial correlation analyses, other potential confounding variables were not included. For instance, factors such as gender, side of implantation, lateralization or the etiology of deafness could have introduced variability in the results. Hearing aid wearing time was also tested but did not show a significant effect.

5.2.2 MRI Data Acquisition and Processing

The diffusion acquisition protocol used in this study included a limited number of diffusion directions, which may reduce the ability to resolve complex fiber architectures and increase the sensitivity to noise [26, 83].

5.2.3 Tractography and Tractometry

White matter tractography, while informative, is subject to a number of limitations. The reconstructed tracts showed inter-subject variability in terms of the number, length, and spatial extent of streamlines, which may introduce noise in group-level comparisons. Moreover, although clustering allowed for standardized analysis across subjects, cluster boundaries may not always correspond anatomically across individuals, despite efforts to ensure consistent orientation and indexing.

Another limitation concerns the uniform subdivision of all tracts into eight groups, irrespective of length, shape or anatomical complexity. This fixed segmentation choice, made for reasons of methodological consistency, may not optimally reflect significant anatomical or functional subdivisions for each tract. An approach that adjusts the number of clusters according to tract geometry could potentially enable a better local analysis.

As highlighted by Takemura et al. (2024) [32], changes in FA profiles may reflect different biological mechanisms beyond demyelination or degeneration. These factors complicate the biological interpretation of diffusion metrics and call for cautious conclusions.

Finally, while the study focused on language, and hearing-related tracts, exploring other brain regions unrelated to auditory processing could strengthen the specificity of the observed findings.

5.2.4 Statistical Considerations

Statistical correction was performed using the FDR method, which controls the proportion of false positives among significant findings. However, it has been demonstrated that FDR controls are less conservative than Family-wise error rate (FWER) controls. This results in a lower false negative rate at the cost of a higher false positive rate [84].

5.3 Perspectives and Future Work

The possibilities for improving and extending this study are directly related to the limitations discussed above. Several strategies could be implemented to strengthen the results and further explore the correlations between neural and CI outcomes:

- **Extension of ROIs:** Future research could benefit from including additional white matter tracts beyond the classical auditory-language pathways. In particular, the inferior longitudinal fasciculus (ILF) and superior longitudinal fasciculus (SLF) deserve further investigation. Ivanova et al. [18] reported that language comprehension was closely associated with the integrity of the ILF. Moreover, Huang et al. [65] found microstructural differences in the SLF and ILF between individuals with hearing loss and controls, suggesting these tracts may also contribute to auditory-cognitive integration.

- **Refinement of weighting strategies:** As highlighted in the Results interpretation section, using streamline density weighting instead of a binary mask to average diffusion metrics may improve sensitivity to microstructural variations.

- **Advanced diffusion imaging techniques:** Employing higher angular resolution diffusion imaging or multi-shell acquisitions would enable more accurate modeling of complex fiber configurations, such as fiber crossing regions, improving tract reconstruction quality and interpretability. For example, using the constrained spherical deconvolution (CSD) model.

- **Multimodal neuroimaging:** Combining structural diffusion imaging with functional MRI could help clarify the relationship between anatomical pathways and functional activation patterns in auditory and language networks.

- **Machine learning approaches:** Future studies could investigate whether predictive models trained on preoperative neuroimaging metrics and clinical variables (e.g., age, duration of hearing loss) could improve outcome forecasting after cochlear implantation. For example, simple classification algorithms could help identify patients most likely to achieve favorable auditory outcomes.

- **Consideration of hemispheric lateralization:** Interindividual variability in lateralization of language or auditory functions may influence CI outcomes and should be accounted for in future analyses [85].

Chapter 6

Conclusion

This study aimed to explore the relationship between the microstructural integrity of specific white matter tracts and auditory performance following cochlear implantation, using diffusion MRI tractography analyses. Significant correlations were identified between DEWA test scores and diffusion metrics measured in the posterior segment of the left AF as well as in the right IFOF, primarily at the pre-operative stage and six months after implantation.

The clustering approach enabled the identification of specific subregions, particularly in the superior temporal gyrus, the inferior parietal lobe, and the external capsule, where better microstructural organization was associated with improved audiovisual comprehension performance. In contrast, no significant associations were observed at twelve months, suggesting a plateau effect in auditory recovery.

The analysis also failed to reveal any relationship between diffusion metrics and the progression of scores over time, which may be explained by ceiling effects in some participants. Moreover, the absence of correlations involving mean FA highlights the limitations of whole-tract averaging and reinforces the relevance of localized analyses.

Nevertheless, this study has certain limitations, including a relatively small sample size, limited diffusion data resolution, and the absence of consideration for hemispheric lateralization and other clinical factors. It paves the way for future research incorporating advanced imaging techniques, multimodal approaches, and more personalized predictive models.

In summary, this thesis highlights the value of targeted tractography for identifying early biomarkers of cochlear implant success, ultimately contributing to better candidate selection and more individualized patient care.

Bibliography

[1] Organisation mondiale de la Santé. *Surdité et perte auditive.* `https://www.who.int/fr/news-room/fact-sheets/detail/deafness-and-hearing-loss`. Consulté le 7 mai 2025. 2024.

[2] Institut National d'Assurance Maladie-Invalidité (INAMI). *Remboursement des implants cochléaires.* `https://www.inami.fgov.be/fr/themes/soins-de-sante-cout-et-remboursement/les-prestations-de-sante-que-vous-rembourse-votre-mutualite/dispositifs-medicaux-materiel-medical/implants-et-dispositifs-medicaux-invasifs/remboursement-des-implants-cochleaires`. Consulté le 10 mai 2025. 2024.

[3] Bruno Kastler and Daniel Vetter. *Comprendre l'IRM: Manuel d'auto-apprentissage.* Google-Books-ID: 2N5LDwAAQBAJ. Elsevier Health Sciences, Mar. 6, 2018. 421 pp. ISBN: 978-2-294-75443-2.

[4] Yusuf Abu Tayeb Bhagat. "Diffusion Tensor Imaging of the Human Brain". Accessed via ResearchGate. PhD Thesis. University of Alberta, 2007.

[5] Hélène Poinsignon-Clique. "Mise en place d'une mesure quantitative du T1 en IRM cardiaque". Thèse de doctorat en Sciences de la Vie et de la Santé, soutenue le 13 novembre 2012. Consulté le 4 mai 2025. PhD thesis. Vandœuvre-lès-Nancy, France: Université de Lorraine, 2012.

[6] IMAIOS. *Spin Echo.* `https://www.imaios.com/en/e-mri/sequences/spin-echo`. Accessed: 2025-05-04.

[7] Info-Radiologie.ch. *Imagerie par résonance magnétique (IRM).* `https://info-radiologie.ch/resonance_magnetique.php`. Accessed : 2025-02-27. n.d.

[8] Randa Boukabene et al. "Segmentation des IRM-3D en utilisant les champs aléatoires de Markov cachés et cuckoo search technique." PhD thesis. Sept. 9, 2020. DOI: `10.13140/RG.2.2.20256.61446`.

[9] C. Oppenheim et al. “Imagerie en tenseur de diffusion et tractographie de l’encéphale et de la moelle”. In: *Journal de Radiologie*. FMC - Innovation en neuro-imagerie 88.3 (Mar. 1, 2007), pp. 510–520. ISSN: 0221-0363. DOI: 10.1016/S0221-0363(07)89850-7.

[10] Roland Bammer. “Basic principles of diffusion-weighted imaging”. In: *European Journal of Radiology* 45.3 (2003). Consulté le 4 mai 2025, pp. 169–184. DOI: 10.1016/S0720-048X(02)00303-0.

[11] *Diffusion-weighted imaging | Radiology Reference Article | Radiopaedia.org*. URL: https://radiopaedia.org/articles/diffusion-weighted-imaging-2?embed_domain=hackmd.io/@yipuafecsl2jsu8smr5njq/bnjhjgjghjghjgh&lang=us (visited on 04/28/2025).

[12] MRI Questions. *What is the b-value?* https://mriquestions.com/what-is-the-b-value.html. accessed : 2025-04-08.

[13] Lauren J. O’Donnell and Carl-Fredrik Westin. “An introduction to diffusion tensor image analysis”. In: *Neurosurgery clinics of North America* 22.2 (Apr. 2011), pp. 185–viii. ISSN: 1042-3680. DOI: 10.1016/j.nec.2010.12.004.

[14] Wikipedia contributors. *Diffusion-weighted magnetic resonance imaging*. https://en.wikipedia.org/w/index.php?title=Diffusion-weighted_magnetic_resonance_imaging&oldid=1259440787. accessed : 2025-03-25. 2024.

[15] Yuki Saito, Hiroshi Saito, and Takashi Yamamoto. “Anatomo-functional profile of white matter tracts in relevance to language processing: A systematic review”. In: *Brain and Development* 45.6 (2023). accessed : 2025-02-27, pp. 353–364. DOI: 10.1016/j.braindev.2023.02.005.

[16] Do Tromp. *The diffusion tensor, and its relation to FA, MD, AD and RD*. https://www.diffusion-imaging.com/2015/10/what-is-diffusion-tensor.html. accessed : 2025-04-04. 2015.

[17] Sabine Hofer and Jens Frahm. “Topography of the human corpus callosum revisited—Comprehensive fiber tractography using diffusion tensor magnetic resonance imaging”. In: *NeuroImage* 32.3 (Sept. 1, 2006), pp. 989–994. ISSN: 1053-8119. DOI: 10.1016/j.neuroimage.2006.05.044.

[18] Maria V. Ivanova et al. “Diffusion-tensor imaging of major white matter tracts and their role in language processing in aphasia”. In: *Cortex* 85 (Dec. 1, 2016), pp. 165–181. ISSN: 0010-9452. DOI: 10.1016/j.cortex.2016.04.019.

[19] “Artifacts”. In: *MRI Basic Principles and Applications*. Section: 9 _eprint: https://onlinelibrary.wiley.com/doi/pdf/10.1002/9781119013068.ch9. John Wiley & Sons, Ltd, 2015, pp. 103–125. ISBN: 978-1-119-01306-8. DOI: 10.1002/9781119013068.ch9.

[20] Jesper L. R. Andersson and Stamatios N. Sotiropoulos. "An integrated approach to correction for off-resonance effects and subject movement in diffusion MR imaging". In: *NeuroImage* 125 (Jan. 15, 2016), pp. 1063–1078. ISSN: 1053-8119. DOI: `10.1016/j.neuroimage.2015.10.019`.

[21] M Jenkinson et al. "FSL". In: *NeuroImage* 62.2 (2012), pp. 782–790.

[22] SM Smith et al. "Advances in functional and structural MR image analysis and implementation as FSL". In: *NeuroImage* 23.S1 (2004), pp. 208–219.

[23] Logan R. Ranzenberger, Joe M. Das, and Travis Snyder. "Diffusion Tensor Imaging". In: *StatPearls*. Treasure Island (FL): StatPearls Publishing, 2025.

[24] J-Donald Tournier, Fernando Calamante, and Alan Connelly. "MRtrix: Diffusion tractography in crossing fiber regions". In: *International Journal of Imaging Systems and Technology* 22.1 (2012). _eprint: https://onlinelibrary.wiley.com/doi/pdf/10.1002/ima.22005, pp. 53–66. ISSN: 1098-1098. DOI: `10.1002/ima.22005`.

[25] Nuno Loução and Rita Nunes. *Human brain tractography: A DTI vs DKI comparison analysis*. `https://www.researchgate.net/publication/301408677_Human_brain_tractography_A_DTI_vs_DKI_comparison_analysis`. accessed : 2025-05-05. 2016.

[26] Ben Jeurissen et al. "Diffusion MRI fiber tractography of the brain". In: *NMR in Biomedicine* 32.4 (2019). _eprint: https://onlinelibrary.wiley.com/doi/pdf/10.1002/nbm.3785, e3785. ISSN: 1099-1492. DOI: `10.1002/nbm.3785`.

[27] Ahmed Abdrabou. *Diffusion tensor imaging and fiber tractography | Radiology Reference Article | Radiopaedia.org*. Radiopaedia. DOI: `10.53347/rID-22702`. URL: `https://radiopaedia.org/articles/diffusion-tensor-imaging-and-fiber-tractography-1` (visited on 04/08/2025).

[28] Hangyi Jiang et al. "DtiStudio: Resource program for diffusion tensor computation and fiber bundle tracking". In: *Computer Methods and Programs in Biomedicine* 81.2 (Feb. 1, 2006), pp. 106–116. ISSN: 0169-2607. DOI: `10.1016/j.cmpb.2005.08.004`.

[29] B. W. Kreher, I. Mader, and V. G. Kiselev. "Gibbs tracking: a novel approach for the reconstruction of neuronal pathways". In: *Magnetic Resonance in Medicine* 60.4 (Oct. 2008), pp. 953–963. ISSN: 1522-2594. DOI: `10.1002/mrm.21749`.

[30] Ylva Lilja et al. "Visualizing Meyer's loop: A comparison of deterministic and probabilistic tractography". In: *Epilepsy Research* 108.3 (Mar. 1, 2014), pp. 481–490. ISSN: 0920-1211. DOI: `10.1016/j.eplepsyres.2014.01.017`.

[31] Jennifer Muller et al. “Clinically applicable delineation of the pallidal sensorimotor region in patients with advanced Parkinson’s disease: Study of probabilistic and deterministic tractography”. In: *Journal of Neurosurgery* (Dec. 14, 2018), pp. 1–12. DOI: `10.3171/2018.7.JNS18541`.

[32] Hiromasa Takemura et al. “Tractometry of Human Visual White Matter Pathways in Health and Disease”. In: *Magnetic Resonance in Medical Sciences* 23.3 (June 12, 2024), pp. 316–340. ISSN: 1347-3182. DOI: `10.2463/mrms.rev.2024-0007`.

[33] Frontiers in Neuroscience. *Methods and Applications of Diffusion MRI Tractometry*. `https://www.frontiersin.org/research-topics/56719/methods-and-applications-of-diffusion-mri-tractometry`. accessed : 2025-05-06. 2024.

[34] Andrew L. Alexander et al. “Characterization of Cerebral White Matter Properties Using Quantitative Magnetic Resonance Imaging Stains”. In: *Brain Connectivity* 1.6 (Dec. 2011), pp. 423–446. ISSN: 2158-0014. DOI: `10.1089/brain.2011.0071`.

[35] Yingrong Xie et al. “Enhanced Integrity of White Matter Microstructure in Mind–Body Practitioners: A Whole-Brain Diffusion Tensor Imaging Study”. In: *Brain Sciences* 13.4 (Apr. 2023). Number: 4 Publisher: Multidisciplinary Digital Publishing Institute, p. 691. ISSN: 2076-3425. DOI: `10.3390/brainsci13040691`.

[36] Anthony A. Mercadante and Prasanna Tadi. “Neuroanatomy, Gray Matter”. In: *StatPearls*. Treasure Island (FL): StatPearls Publishing, 2025.

[37] Marco Catani, Derek K. Jones, and Dominic H. Ffytche. “Perisylvian Language Networks of the Human Brain”. In: *Annals of Neurology* 57.1 (2005), pp. 8–16. DOI: `10.1002/ana.20319`.

[38] Andrew K Conner et al. “A Connectomic Atlas of the Human Cerebrum—Chapter 13: Tractographic Description of the Inferior Fronto-Occipital Fasciculus”. In: *Operative Neurosurgery* 15 (Suppl 1 Dec. 2018), S436–S443. ISSN: 2332-4252. DOI: `10.1093/ons/opy267`.

[39] Guillaume Herbet, Sylvie Moritz-Gasser, and Hugues Duffau. “Direct evidence for the contributive role of the right inferior fronto-occipital fasciculus in non-verbal semantic cognition”. In: *Brain Structure & Function* 222.4 (May 2017), pp. 1597–1610. ISSN: 1863-2661. DOI: `10.1007/s00429-016-1294-x`.

[40] ScienceDirect. *Anomia – ScienceDirect Topics*. `https://www.sciencedirect.com/topics/nursing-and-health-professions/anomia`. accessed : 2025-03-04.

[41] Kylie H. Alm et al. “Fronto-temporal white matter connectivity predicts reversal learning errors”. In: *Frontiers in Human Neuroscience* 9 (June 18, 2015). Publisher: Frontiers. ISSN: 1662-5161. DOI: `10.3389/fnhum.2015.00343`.

[42] Stephanie Forkel et al. *Dissecting white matter pathways: A neuroanatomical approach*. Aug. 9, 2023. DOI: `10.31234/osf.io/9xwgm`.

[43] Rebecca J. Von Der Heide et al. “Dissecting the uncinate fasciculus: disorders, controversies and a hypothesis”. In: *Brain* 136.6 (June 2013), pp. 1692–1707. ISSN: 0006-8950. DOI: `10.1093/brain/awt094`.

[44] Juliana S. Bloom and George W. Hynd. “The Role of the Corpus Callosum in Interhemispheric Transfer of Information: Excitation or Inhibition?” In: *Neuropsychology Review* 15.2 (June 1, 2005), pp. 59–71. ISSN: 1573-6660. DOI: `10.1007/s11065-005-6252-y`.

[45] Andrea Goldstein et al. “Neuroanatomy, Corpus Callosum”. In: *StatPearls*. Treasure Island (FL): StatPearls Publishing, 2025.

[46] DÁVI. *Ear Anatomy*. `https://davi.pt/en/otorhinolaryngology/ear-anatomy`. Accessed: 2025-05-04.

[47] MediaHouse GmbH. *The route of sound through the cochlea*. `https://medienportal.siemens-stiftung.org/en/the-route-of-sound-through-the-cochlea-102092`. accessed : 04-05-2025. Siemens Stiftung, 2016.

[48] *Les Cahiers de l’Audition – Numéro 1, 2011*. `https://www.college-nat-audio.fr/sites/default/files/cahier_audition_pdf/2011-1.pdf`. 2011.

[49] Pujol, Rémy. *Auditory Brain*. `https://www.cochlea.eu/en/auditory-brain/`. accessed : 2025-05-02. 2024.

[50] Dale Purves et al. “The Auditory Cortex”. In: *Neuroscience. 2nd edition*. Sinauer Associates, 2001.

[51] Centers for Disease Control and Prevention. *Types of Hearing Loss*. `https://www.cdc.gov/hearing-loss-children/about/types-of-hearing-loss.html`. accessed : 2025-02-05. 2024.

[52] Roddy Cowie and Ellen Douglas-Cowie. *Postlingually Acquired Deafness: Speech Deterioration and the Wider Consequences*. Google-Books-ID: jVYyB6CtvfcC. Walter de Gruyter, June 1, 2011. 317 pp. ISBN: 978-3-11-086912-5.

[53] Olivier Macherey and Robert P. Carlyon. “Cochlear implants”. In: *Current Biology* 24.18 (Sept. 22, 2014). Publisher: Elsevier. ISSN: 0960-9822. DOI: 10.1016/j.cub.2014.06.053.

[54] Fan-Gang Zeng. *DEWA, un test d’intégration audiovisuelle*. Publisher: SAGE Publications. Dec. 1, 2004. URL: https://audiologie-demain.com/dewa-un-test-dintegration-audiovisuelle (visited on 02/04/2025).

[55] Children’s Nebraska. *About Cochlear Implants*. https://www.childrensnebraska.org/about-cochlear-implants. accessed : 2025-02-04.

[56] *Audiogramme : comment le lire et le comprendre ? Guide complet / VivaSon*. URL: https://www.vivason.fr/votre-audition/test-auditif/lire-audiogramme?srsltid=AfmB0oqfanooa_XiBB_Id2ARlLHqppfhbBbHJI0eCVGEnA9tN26uIPl_ (visited on 02/04/2025).

[57] Commission de la sécurité professionnelle et de l’assurance contre les accidents du travail (WSIB). *Évaluation de l’audition – Formulaire 3275B*. https://www.wsib.ca/sites/default/files/2024-11/3275bhearing_assessment_0223_frenchsecured.pdf. accessed : 2025-05-04. 2023.

[58] Amplifon. *Audiométrie tonale et vocale*. https://www.amplifon.com/fr/etapes-appareillage-auditif/test-d-audition-gratuit/audiometrie-tonale-vocale. accessed : 2024-11-12. 2024.

[59] Polyclinique de l’Oreille. *Audiogramme*. https://www.polycliniquedeloreille.com/test-auditif-complet/audiogramme. accessed : 2025-05-02.

[60] Maria V. Ivanova et al. “Contributions of the arcuate fasciculus to language repetition”. In: *Frontiers in Human Neuroscience* 15 (2021), p. 684306. ISSN: 1662-5161. DOI: 10.3389/fnhum.2021.684306.

[61] Susan Teubner-Rhodes et al. “Aging-Resilient Associations between the Arcuate Fasciculus and Vocabulary Knowledge: Microstructure or Morphology?” In: *The Journal of Neuroscience* 36.27 (2016), pp. 7210–7222. DOI: 10.1523/JNEUROSCI.4342-15.2016.

[62] Yongmin Chang et al. “Voxel-Wise Analysis of Diffusion Tensor Imaging for Clinical Outcome of Cochlear Implantation: Retrospective Study”. In: *Clinical and Experimental Otorhinolaryngology* 5.Suppl 1 (2012), S37–S42. DOI: 10.3342/ceo.2012.5.S1.S37.

[63] Alexandre Roux et al. “Combining Electrostimulation With Fiber Tracking to Stratify the Inferior Fronto-Occipital Fasciculus”. In: *Frontiers in Neuroscience* 15 (May 20, 2021). Publisher: Frontiers. ISSN: 1662-453X. DOI: 10.3389/fnins.2021.683348.

[64] Yiqing Li et al. “Sensitive Period for White-Matter Connectivity of Superior Temporal Cortex in Deaf People”. In: *Human Brain Mapping* 33.2 (2012), pp. 349–359. DOI: 10.1002/hbm.21213.

[65] Ranran Huang et al. “Alterations of the cerebral microstructure in patients with noise-induced hearing loss: A diffusion tensor imaging study”. In: *Brain and Behavior* 14.4 (2024). _eprint: https://onlinelibrary.wiley.com/doi/pdf/10.1002/brb3.3479, e3479. ISSN: 2162-3279. DOI: 10.1002/brb3.3479.

[66] Ying Luan et al. “Prefrontal-Temporal Pathway Mediates the Cross-Modal and Cognitive Reorganization in Sensorineural Hearing Loss With or Without Tinnitus: A Multimodal MRI Study”. In: *Frontiers in Neuroscience* 13 (Mar. 12, 2019), p. 222. ISSN: 1662-4548. DOI: 10.3389/fnins.2019.00222.

[67] Nicole M. Armstrong et al. “Association of Poorer Hearing With Longitudinal Change in Cerebral White Matter Microstructure”. In: *JAMA Otolaryngology–Head & Neck Surgery* 146.11 (Nov. 1, 2020), pp. 1035–1042. ISSN: 2168-6181. DOI: 10.1001/jamaoto.2020.2497.

[68] Raphaële Quatre, Sébastien Schmerber, and Arnaud Attyé. “Improving rehabilitation of deaf patients by advanced imaging before cochlear implantation”. In: *Journal of Neuroradiology* 51.2 (2024), pp. 145–154. DOI: 10.1016/j.neurad.2023.10.002.

[69] Quentin Dessain, SimonMathieu1804, and Nicolas Delinte. *Hyedryn/elikopy: v0.4.6*. Version v0.4.6. doi: 10.5281/zenodo.15174119. Apr. 8, 2025.

[70] Dessain, Quentin and Simon, Mathieu. *Introduction to ElikoPy*. https://elikopy.readthedocs.io/en/latest/introduction.html. accessed : 2025-04-28. 2021.

[71] Jessie Mosso et al. “MP-PCA denoising for diffusion MRS data: promises and pitfalls”. In: *NeuroImage* 263 (Nov. 1, 2022), p. 119634. ISSN: 1053-8119. DOI: 10.1016/j.neuroimage.2022.119634.

[72] Jesper L. R. Andersson, Stefan Skare, and John Ashburner. “How to correct susceptibility distortions in spin-echo echo-planar images: application to diffusion tensor imaging”. In: *NeuroImage* 20.2 (Oct. 2003), pp. 870–888. ISSN: 1053-8119. DOI: 10.1016/S1053-8119(03)00336-7.

[73] N. Tzourio-Mazoyer et al. “Automated Anatomical Labeling of Activations in SPM Using a Macroscopic Anatomical Parcellation of the MNI MRI Single-Subject Brain”. In: *NeuroImage* 15.1 (Jan. 1, 2002), pp. 273–289. ISSN: 1053-8119. DOI: 10.1006/nimg.2001.0978.

[74] Andreas Horn. *MNI T1 6thGen NLIN to MNI 2009b NLIN ANTs transform*. Artwork Size: 208235992 Bytes Pages: 208235992 Bytes. 2016. DOI: 10.6084/M9.FIGSHARE.3502238.V1.

[75] J-Donald Tournier et al. "*MRtrix3*: A fast, flexible and open software framework for medical image processing and visualisation". In: *NeuroImage* 202 (Nov. 15, 2019), p. 116137. ISSN: 1053-8119. DOI: 10.1016/j.neuroimage.2019.116137.

[76] Sabine Hofer and Jens Frahm. "Topography of the human corpus callosum revisited—Comprehensive fiber tractography using diffusion tensor magnetic resonance imaging". In: *NeuroImage* 32.3 (Sept. 1, 2006), pp. 989–994. ISSN: 1053-8119. DOI: 10.1016/j.neuroimage.2006.05.044.

[77] J.-D. Tournier, F. Calamante, and A. Connelly. "Improved probabilistic streamlines tractography by 2nd order integration over fibre orientation distributions". In: *Proceedings of the 18th Annual Meeting of ISMRM*. Stockholm, Sweden, 2010, p. 1670.

[78] Nicolas Delinte. *DelinteNicolas/UNRAVEL: v1.6.4*. Version v1.6.4. Mar. 28, 2025. DOI: 10.5281/zenodo.15100408.

[79] Yoav Benjamini and Yosef Hochberg. "Controlling the False Discovery Rate: A Practical and Powerful Approach to Multiple Testing". In: *Journal of the Royal Statistical Society: Series B (Methodological)* 57.1 (1995). _eprint: https://onlinelibrary.wiley.com/doi/pdf/10.1111/j.2517-6161.1995.tb02031.x, pp. 289–300. ISSN: 2517-6161. DOI: 10.1111/j.2517-6161.1995.tb02031.x.

[80] J.H. McDonald. *Handbook of Biological Statistics*. 3rd. Sparky House Publishing, Baltimore, Maryland, 2014.

[81] Silvio Sarubbo et al. "Mapping critical cortical hubs and white matter pathways by direct electrical stimulation: an original functional atlas of the human brain". In: *NeuroImage* 205 (Jan. 15, 2020), p. 116237. ISSN: 1053-8119. DOI: 10.1016/j.neuroimage.2019.116237.

[82] Margaret T. Dillon et al. "Long-term speech perception in elderly cochlear implant users". In: *JAMA otolaryngology– head & neck surgery* 139.3 (Mar. 2013), pp. 279–283. ISSN: 2168-619X. DOI: 10.1001/jamaoto.2013.1814.

[83] Paween Wongkornchaovalit et al. "Diffusion MRI With High to Ultrahigh b-Values: How It Will Benefit the Discovery of Brain Microstructure and Pathological Changes". In: *Investigative Magnetic Resonance Imaging* 26.4 (Dec. 1, 2022), pp. 200–207. ISSN: 2384-1095. DOI: 10.13104/imri.2022.26.4.200.

[84] R. H. Riffenburgh. “Chapter 15 - Managing Results of Analysis”. In: *Statistics in Medicine (Third Edition)*. Ed. by R. H. Riffenburgh. San Diego: Academic Press, Jan. 1, 2012, pp. 325–343. ISBN: 978-0-12-384864-2. DOI: `10.1016/B978-0-12-384864-2.00015-9`.

[85] M.W. Vernooij et al. “Fiber density asymmetry of the arcuate fasciculus in relation to functional hemispheric language lateralization in both right- and left-handed healthy subjects: A combined fMRI and DTI study”. In: *NeuroImage* 35.3 (2007), pp. 1064–1076. DOI: `10.1016/j.neuroimage.2006.12.041`.

Appendix A

Comportemental data

The figure A.1 illustrates the distribution of participant ages at the time of cochlear implantation, as well as the duration of hearing aid use prior to implantation. These descriptive data help characterize the clinical population included in the study.

Although Spearman's correlation was used for the statistical analysis, linear regression plots are presented in Figures A.2 and A.3 to visually illustrate the trends observed in the data.

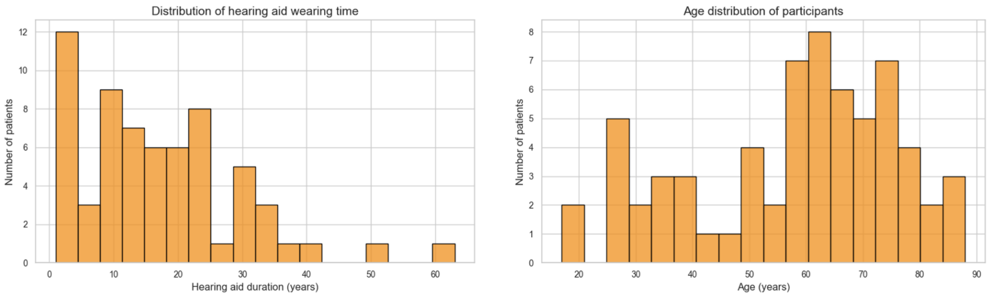

Figure A.1: Left: distribution of hearing aid use duration prior to implantation. Right: distribution of participant ages at the time of cochlear implantation.

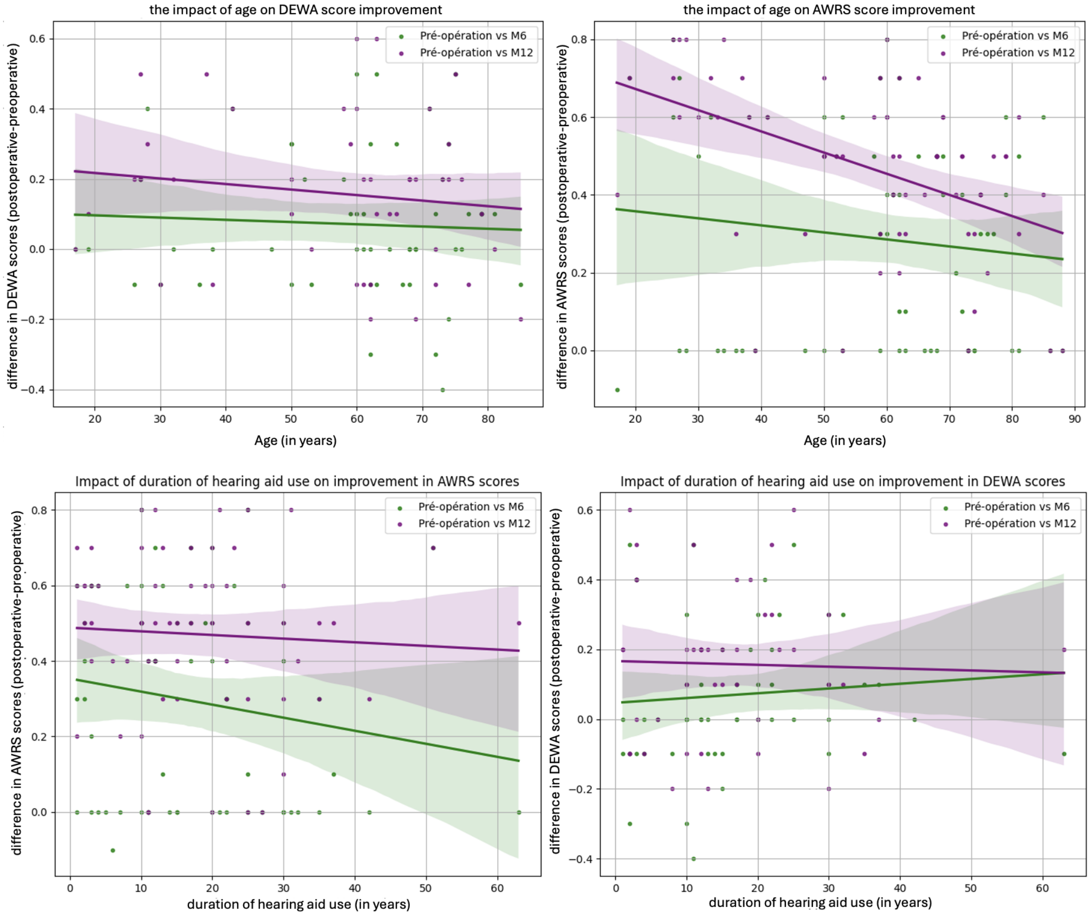

Figure A.2: Impact of age and hearing aid use on post-operative improvements in audiometric scores. Linear regressions were computed to assess the relationship between patient age or duration of hearing aid use (x-axis) and improvement in speech perception performance (y-axis), measured as the difference between preoperative and postoperative scores. The top row shows the effect of age on DEWA (left) and AWRS (right) improvements, while the bottom row displays the effect of hearing aid use duration on AWRS (left) and DEWA (right) improvements.

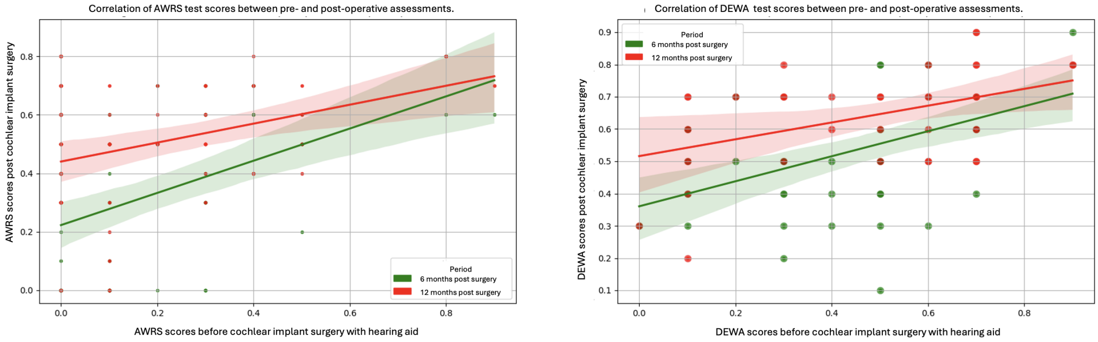

Figure A.3: Correlation between preoperative and postoperative audiometric scores.

A.1 Audiometric Variable Definitions

Table A.1: Audiometric variables used in statistical analyses

Variable	**Description**
AWRS_pre	AWRS score before cochlear implantation
AWRS_preHA	AWRS score before cochlear implantation with hearing aid
AWRS_6m	AWRS score at 6 months after cochlear implantation
AWRS_12m	AWRS score at 12 months after cochlear implantation
DEWA_preHA	DEWA audiovisual score before implantation with hearing aid
DEWA_6m	DEWA audiovisual score at 6 months after cochlear implantation
DEWA_12m	DEWA audiovisual score at 12 months after cochlear implantation
diff_dewa_6m	DEWA audiovisual score evolution between pre-implantation and 6 months after cochlear implantation
diff_dewa_12m	DEWA audiovisual score evolution between pre-implantation and 12 months after cochlear implantation

Appendix B

Preprocessing

Table B.1: Summary of diffusion MRI preprocessing steps, the tools used, and their objectives.

Step	**Tool / Method**	**Purpose**
Brain extraction (skull stripping)	Elikopy (FSL BET)	Remove non-brain tissue to isolate cerebral structures
Resampling to isotropic resolution	Elikopy internal resampling	Standardize voxel size to $2 \times 2 \times 2$ mm^3 to reduce interpolation artifacts
Denoising	MPPCA	Reduce thermal (Rician) noise
Eddy current correction	FSL Eddy	Correct for distortions caused by gradient-induced eddy currents
Susceptibility distortion correction	FSL Topup (with T1-weighted image)	Correct B_0 field inhomogeneity
Diffusion modeling	DTI (Elikopy)	Compute scalar diffusion metrics: FA, MD, AD, RD

Appendix C

Tractography

Here are the representations on Figure C.2 for the CC, on Figure C.3 for the AF and on Figure C.1 for the IFOF and UF of the 3D coordinate of the first and last clusters of each tract to verify that the cluster numbering follows the same direction for all subjects, and if not, to manually invert the data.

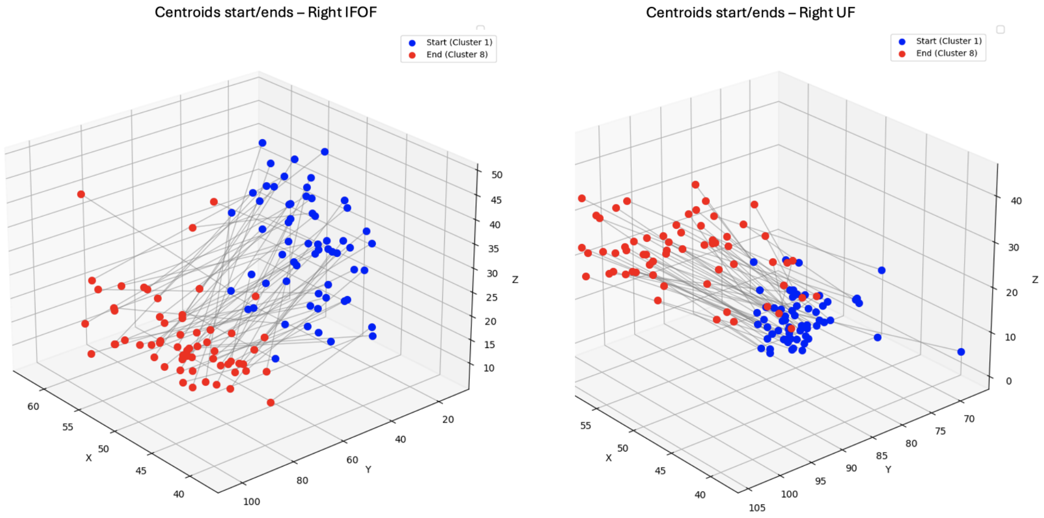

Figure C.1: Verification of cluster orientation for the right UF segment and the right IFOF. For each subject, the centroid of the first cluster is shown in blue and the last cluster in red.

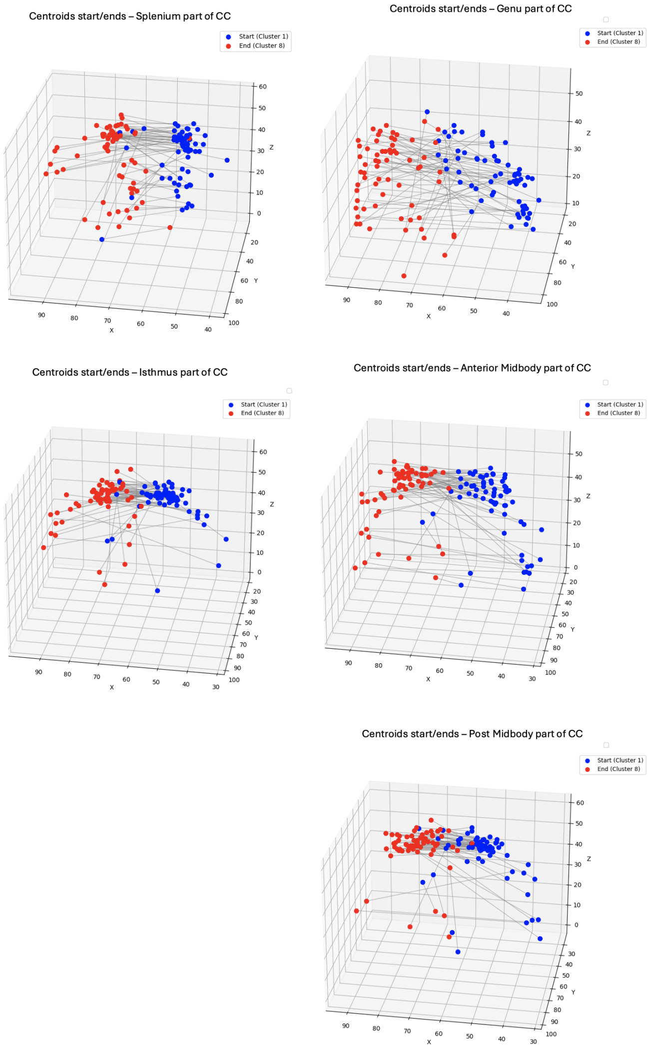

Figure C.2: Verification of cluster orientation for the five segments of CC. For each subject, the centroid of the first cluster is shown in blue and the last cluster in red.

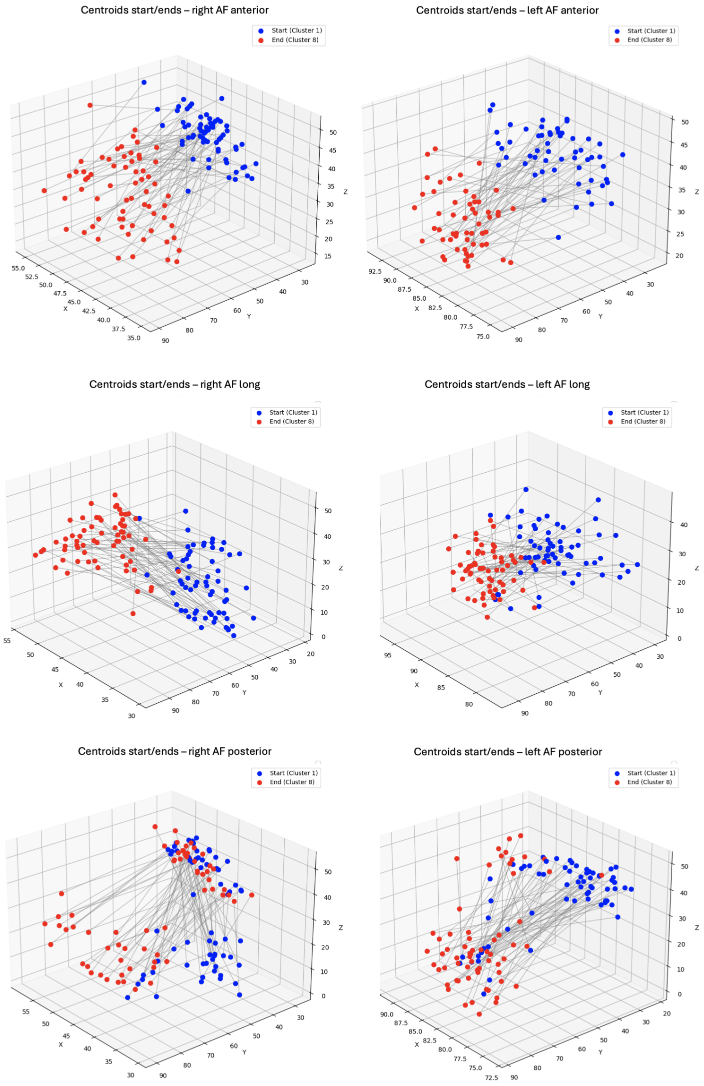

Centroids start/ends – right AF anterior

Centroids start/ends – left AF anterior

Centroids start/ends – right AF long

Centroids start/ends – left AF long

Centroids start/ends – right AF posterior

Centroids start/ends – left AF posterior

Figure C.3: Verification of cluster orientation for the six segments of the arcuate fasciculus: left and right long, anterior, and posterior AF. For each subject, the centroid of the first cluster is shown in blue and the last cluster in red.

UNIVERSITÉ CATHOLIQUE DE LOUVAIN
École polytechnique de Louvain
Rue Archimède, 1 bte L6.11.01, 1348 Louvain-la-Neuve, Belgique | **www.uclouvain.be/epl**